Resolving the porosity-unmelted inclusion dilemma during *in-situ* alloying of Ti34Nb via Laser Powder Bed Fusion

Sheng Huang [a], R. Lakshmi Narayan[b#], Joel Heang Kuan Tan[a], Swee Leong Sing[a] and Wai Yee Yeong [a#]

[a]Singapore Centre for 3D Printing, School of Mechanical & Aerospace Engineering, Nanyang Technological University, 50 Nanyang Avenue, Singapore 639798

[b]Department of Materials Science and Engineering, Indian Institute of Technology, Delhi, Hauz Khas, New Delhi, India 110016

#address for correspondence: wyyeong@ntu.edu.sg, rlnarayan@iitd.ac.in

Keywords: Mechanical properties, Titanium alloy, Finite element analysis, Ti–Nb, Powder bed fusion

A parametric experimental study on the role played by the power (P), velocity (V_L) and profile (top hat or Gaussian) of the laser on the porosity, inclusion content and microstructural evolution of *in-situ* alloyed laser powder bed fusion (LPBF) manufactured Ti34Nb was conducted. For this, alloys were printed with three sets of processing parameters, in which the above-mentioned parameters were varied but the energy density was held constant. A detailed tomographic and microstructural investigation of these alloys was followed by tensile tests. Observations of melt pools in the single tracks and single stripes were complemented by thermal finite element method (FEM) simulations that studied their evolution. Results show

that a top hat laser profile combined with high P (> 650 W), high V_L (> 650 mm/s) and short stripe width scanning strategy forms a large single stripe melt pool that moves slowly and has a low aspect ratio. The large and slow melt pool allows Nb to melt efficiently and minimizes its unmelted content while the low melt pool aspect ratio prevents keyholing that can otherwise result in porosity. These melt pool attributes also favor the formation of a columnar β-Ti microstructure with a strong {100} texture, which has the ideal combination of strength and elastic modulus. The mechanisms of microstructural evolution were explained and the scope of this parameter optimization principle was discussed in the context of further improving the properties of this alloy.

1. Introduction

TiNb alloys are considered promising materials for making biological implants that support and strengthen broken bones in the human body. While conventional implant materials such as 316L stainless steel, CoCrMo and Ti6Al4V are still popular, alternatives are being explored after it was discovered that they indirectly cause osteopenia in recovering bones [1]. The onset of osteopenia -- a condition where the bone tissue does not acquire the appropriate density after healing — due to implant insertion is attributed to the significantly stiffer implant material that completely shields the bone from stress, which is otherwise essential for its growth [1, 2]. An ideal implant material is one whose elastic modulus, E, matches, or is at least reasonably close to that of bone. Cortical bones have E ~30 GPa, whereas all the above-mentioned conventional implant materials have E > 100 GPa [3]. In contrast, TiNb alloys are more appealing as their E ranges from 30 to 65 GPa, depending on the Nb concentration. Note that besides selecting materials with lower E, the stiffness of the implant can also be minimized by geometrical means, i.e., by designing a compliant lattice structure. However, the optimization of implant stiffness via geometrical means is a separate area of research and will hence not be addressed in our study.

An additional advantage of TiNb alloys as an implant material is that the constituents are non-toxic, whereas Ni in stainless steel, Co and Cr in CoCrMo and Al/V in Ti6Al4V are associated with cytotoxicity [4].

Although TiNb alloys have low *E*, they can only be considered structurally viable for implant applications if they possess reasonable strength and toughness. The key requirements to satisfy these conditions are (a) a single phase β-Ti microstructure, which is the toughest phase in Ti alloys (b) a texture that ensures minimum *E*, and (c) a strengthening mechanism that ensures high yield strength. A recent study reported that a cold rolled and annealed Ti33Nb4Sn (wt. %) alloy has the ideal combination of low *E* ~36 GPa and high strength of 853 MPa due to a fine grained β-Ti microstructure with high dislocation density. Employing similar conventional processing techniques, implants manufactured from Ti13Nb13Zr and Ti29Nb13Ta4.6Zr are already commercially available [5, 6]. However, switching to additive manufacturing (AM) technologies, such as laser powder bed fusion (LPBF), to develop these implants is a more attractive alternative as the process is significantly more cost effective, time efficient and recycling friendly [7]. In LPBF, also referred to as selective laser melting (SLM), a component is built incrementally by a high-power laser, which fuses the powders of a material layer-by-layer. The method offers customizability of design and the option of tuning process parameters such as, laser power, scan speed, scanning patterns, etc. to develop specific microstructural features that suit a particular need [8-14]. It is also specifically suited for making TiNb implants, as the fast cooling cycles, intrinsic to the LPBF process, is ideal for obtaining a fine microstructure and retaining metastable β-Ti phase at room temperatures.

Despite these benefits, LPBF fabrication of TiNb alloy implants is limited by the unavailability of printable pre-alloyed powders of specific compositions. To resolve this drawback, several studies have attempted to manufacture Ti-based alloys using the *in-situ* alloying method [15-19]. In this method, the required proportions of two constituent powders are mixed, fed through

the hopper, spread over the powder bed and scanned by laser to obtain the alloyed component. Although *in-situ* alloying is cost effective and conceptually trivial, it has the following drawback associated with it. Since the constituents are expected to have different melting points, it is unlikely that the two would melt uniformly when scanned with the same laser power. Typically, one of the constituents either vaporizes or segregates as an un-melted inclusion in the alloy. In TiNb alloys the latter situation is often encountered. Some studies suggested that the content of un-melted Nb can be reduced by increasing the volumetric energy density, E_d [20, 21]. E_d is related to the laser power, P, laser scanning speed, V_L, distance between two laser scan tracks (also known as hatch spacing), h, and powder layer thickness, t, by the following equation:

$$E_d = \frac{P}{V_L . h . t}, \quad (1)$$

Based on Eq. (1), P must be increased while all the other parameters must be minimized to increase E_d. However, it was observed that while a progressively higher E_d is effective in reducing the content of un-melted Nb, it leads to the formation of keyhole induced porosity in the alloy, which is also an undesirable defect. This conundrum, referred to as the porosity-inclusion dilemma, which is also observed in other Ti based alloys such as TiTa, has not been resolved by optimization strategies that vary E_d, although a few have been tried [20-22]. It was also noted that while E_d is a good measure of the energy density input during printing, it does not consider the subtle variations associated with material-laser interactions, and hence becomes an empirical method to predict build characteristics. To compensate for this, a normalized enthalpy optimization strategy, which involves material as well as printing parameters in LPBF, was developed [23]. However, the application of this strategy in the case of in-situ alloying was unsuccessful as the formulation does not consider the effect of multiple constituent powders [22]. Moreover the normalised enthalpy approach does not capture the re-

melting effect of adjacent laser scans as the influence of hatch spacing is not incorporated in the equation. Considering the limited success of this method in the context of in-situ alloying via LPBF, E_d has been the de-facto standard when it comes to process optimization for the in-situ alloying process. Some other studies partially resolved the porosity-inclusion dilemma and reduced the content of unmelted inclusion, at a fixed porosity content, by employing the laser re-scanning/re-melting technique, where at least twice the number of scans are performed on each layer to ensure better mixing of the constituents [15, 22]. However, this method significantly increases the printing time and energy consumption, which translates to a higher average cost per part.

In this paper, we demonstrate that an alternate strategy of focussing on the melt pool characteristics and dynamics, instead of E_d optimization, is the real key to resolving the porosity-inclusion dilemma in LPBF printed TiNb alloys. For this, samples were built with three different printing parameter sets, where P and V_L were varied while h and t were held constant. P and V_L were also varied in the same proportion, i.e. their ratios were the same in all parameter sets, to ensure invariance of E_d. In addition, the effect of two different laser profiles, namely the Gaussian and top-hat, and influence of the stripe scanning strategy were also considered. The quality of samples was examined via X-ray computed tomography (XCT), the microstructural characterization was performed with scanning electron microscopy (SEM) and electron backscatter diffraction (EBSD) and, the mechanical properties were assessed by conducting uniaxial tension tests. Results of these investigations show that a combination of highest P and V_L, short stripe width scanning strategy and a top hat laser profile produces a fully dense TiNb alloy with a minimal volume fraction of unmelted Nb. Moreover, the microstructure of the sample printed with this parameter set has the optimum microstructure for superior mechanical performance -- β-Ti columnar grains and a dominant {100} texture along the build direction. Using direct visualization of single tracks and single stripes,

complemented by a simple thermal finite element method (FEM) simulation of the latter, we argue that optimizing the dynamics and dimensions of the melt pool, which is facilitated by appropriate parameter optimization -- is necessary for printing defect free, high quality TiNb implants.

2. Experimental details

2.1. Laser powder bed fusion

Samples were fabricated using an in-house developed TiNb elemental powder blends with 34 wt.% Nb. The Ti34Nb powder blend was obtained by mixing spherical gas atomized commercially pure titanium (CP Ti) and Nb powders (> 99.8%). The CP Ti powder (Grade 2 ASTM B348, LPW Technology Ltd, United Kingdom) particles have a median diameter of 43.5 μm while the Nb powder (Tecnisco Advance Material Pte Ltd, Singapore) has a particle size distribution that ranges between 20 to 63 μm. The two elemental powders were mixed and blended for 12 hours at a rate of 30 rpm using a tumbler mixer (Inversina 2 L, Bioengineering AG). The blending process was conducted under an argon quenched atmosphere.

The sample fabrication process was carried out using the SLM 250 HL machine (SLM Solutions Group AG). The machine was customized to be equipped with 2 fibre laser types, as shown in Figure 1a. One of the fibre lasers is conventionally available in many other LPBF machines, which is a Gaussian beam profile laser (1064 nm) with a focus diameter of 80 μm and a maximum laser power of 400 W. The second equipped fiber laser (1064 nm) has a top-hat profile with a focus diameter of 200 μm and a maximum laser power of 1000 W. All fabrication processes were carried out in an argon environment of < 500 ppm oxygen to prevent oxidation and interstitial element contaminations. The samples were built on Ti base plates with area dimensions of 100×100 mm^2. Also, all samples were prepared using the same E_d input and rotated stripe scanning strategy but with different P and V_L. The schematic of a single

track and stripe pattern is shown in Figure 1b. While a single track involves laser scan movement along one direction, a stripe pattern consists of anti-parallel scan vectors, which raster and create a scanned patch that has a much larger width than a single track (blue dashed line in Figure 1b). Each layer is built by a series of parallel stripes that spans its entire length. A schematic of the rotated stripe scanning strategy is shown in Figure 1c. In every subsequent new layer, the stripes rotate clockwise by ~79° with respect to the previous layer. The details of scanning parameters associated with each sample can be seen in Table 1. Note that the samples will hitherto be referred to by the corresponding applied *P* used for printing them, i.e. 350W, 650W and 950W. The laser profile of sample 350W is Gaussian, whereas those of the other two are top-hat.

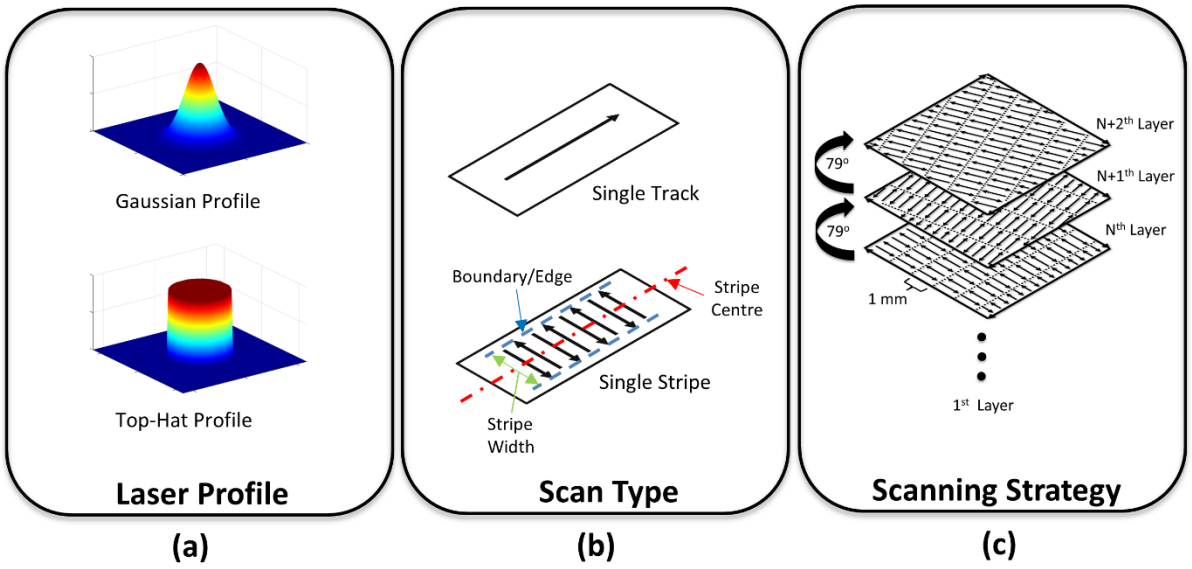

Figure 1. Schematic representations of (a) Gaussian and top hat laser profiles, (b) Schematic of single track and single stripe scanning and (c) The scanning strategy employed. The black arrow in (b) indicates the laser scan paths and directions associated with each scan type.

Table 1 Different combinations of LPBF process parameters utilized for manufacturing the TiNb alloy samples.

Sample name	**Power, *P* (W)**	**Hatch, *h* (µm)**	**Stripe Width (mm)**	**Scanning Velocity, V_L (mm/s)**	**Layer Thickness, *t* (µm)**	**Rotation (°)**	**Energy Density, E_d (W/mm^3)**	**Laser Profile**
350W	350	80	1	350	50	79	350	Gaussian (80 µm)

650W	650	80	1	650	50	79	350	Top-Hat (200 µm)
950W	950	80	1	950	50	79	350	Top-Hat (200 µm)

2.2. Sample Evaluation

The percentage porosity and percentage of un-melted Nb in fabricated samples were analysed via X-ray computed tomography (XCT, Bruker, Germany). X-ray scanning was performed at a voltage of 130 kV using a brass filter. The 3D reconstructed volumes are made up of isotropic cube voxels with a side length of 5.7 µm. Only pores/inclusions with at least 9 voxels were considered to minimize the probability of false segmentation. 3 threshold values were taken during the analysis to account for the error [24] and the standard error was obtained. The sphericity, Ψ of each pore/particle was determined from:

$$\psi = \frac{6 \cdot \pi^{\frac{1}{2}} \cdot \Phi}{\Pi^{\frac{3}{2}}}, \quad (2)$$

where Φ is the volume and Π is the surface area of a pore/inclusion. Archimedes principle was used to measure the density and the surface melt pool characteristics of the samples were examined using confocal microscopy (Confocal microscope, Keyence, Japan). The surface profile for as-printed samples was scanned using a height pitch of 0.1 µm.

2.3. Metallographic Characterization

The samples were sectioned to reveal the cross-sectional area parallel and perpendicular to the build direction (BD). Grit #320 SiC-paper were then used to grind the cross-sections followed by a fine grinding with MD-Largo (DiaPro Largo 9 µm suspension, Struers). Finally, the samples were polished to a mirror finish using MD-Chem (OPS 0.04 µm suspension + H_2O_2, Struers). Optical microscopy (OM) was employed to assess the quality of the surface finish after polishing. The identification of constituent phases in all samples were done by analysing

each sample with X-ray diffraction (XRD, PANalytical Empyrean, Netherlands) using Cu-Kα radiation and a step size of 0.01°. Microstructural characterization was conducted with a field emission scanning electron microscope (FESEM, JEOL 7600F, JEOL, Japan) equipped with a backscatter electron (BSE) detector. Energy dispersive X-Ray spectroscopy (EDS) was done to ascertain the composition of phases. Texture analysis was done with electron backscattering diffraction (EBSD) analysis using FESEM equipped with an AZtecHKL Oxford detector. The EBSD mapping was conducted with a scanning step size of 1.5 μm.

2.4. Finite Element Method (FEM) simulation

A simple thermal simulation was performed for a single stripe scan using the finite element method (FEM) function in COMSOL Multiphysics to model the melt pool geometry and its evolution as a function of the laser scanning parameters in the LPBF process. The solver analyses the laser-powder interaction at 350W and 950W to obtain the temperature history of the powder and substrate. The temperature evolution due to thermal conduction, convection and radiation were obtained by solving the following equations:

$$Q = \rho c_p \frac{\partial T}{\partial t} - \nabla \cdot (K \nabla T), \tag{3}$$

$$q_{conv} = h(T - T_0), \tag{4}$$

$$q_{rad} = \sigma \varepsilon (T^4 - T_0^4), \tag{5}$$

Where, Q is the heat input, q_{conv} is the convective heat lost due to argon gas flow, q_{rad} is the radiative heat loss, ρ is the density, c_p is the specific heat capacity, K is the heat conductivity, h is the convection heat transfer coefficient (~0.25), σ is the Stefan-Boltzmann constant, ε (~0.45) is the emissivity and T_o (~293.15 K) is the ambient temperature. Radiative and convective heat loss are considered on the top surface as the boundary conditions, whereas all the other surfaces are thermally insulated. The size of the model is chosen to be sufficiently

large such that the effect of heat accumulation at the insulated model boundaries does not affect the melt pool formation. Meshing was performed with 12663 brick elements with maximum and minimum feature size of 75 µm and 25 µm respectively. Mesh convergence analysis confirmed that further mesh refinement has insignificant effect on melt pool formation. Time step for 350W and 950W were set at 10 and 30 µs respectively. A schematic of this meshed model is shown in Figure 2.

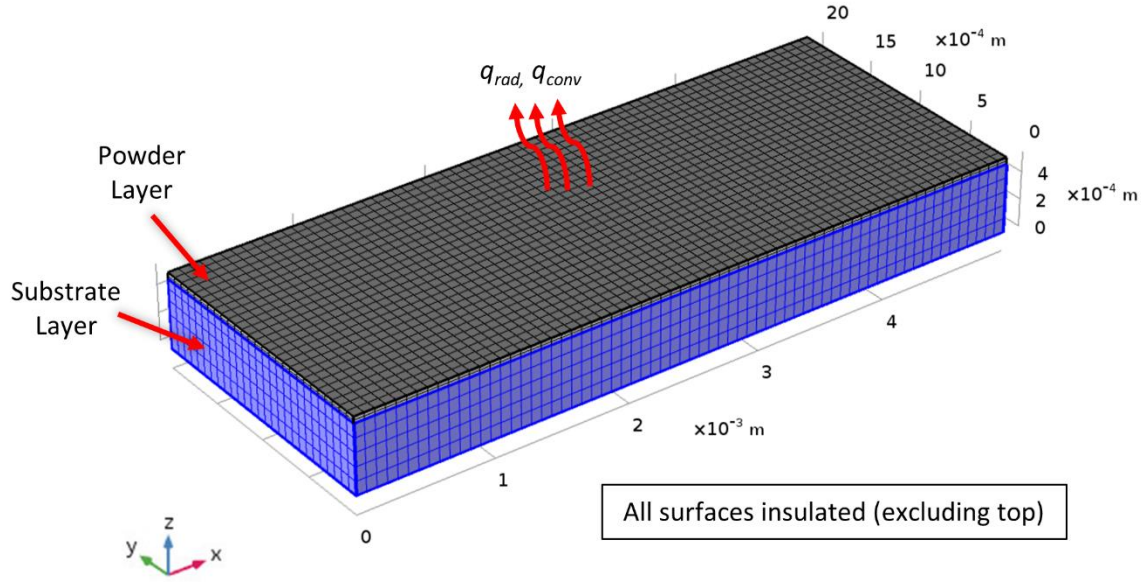

Figure 2 Schematic of model to study melt pool evolution during laser scanning.

For the gaussian and top-hat distributions laser beam profiles, Q is estimated from a volumetric heat source that is based on the Beer Lambert's law [25]:

$$Q_{Gaussian} = \frac{2AP}{\pi r_0^2 S} \exp\left(-\frac{2(x^2 - y^2)}{r_0^2}\right) \exp\left(\frac{-|\lambda - z|}{S}\right), \quad (6)$$

$$Q_{Top\ Hat} = \frac{2AP}{\pi r_0^2 S} \exp\left(-\frac{2(x^2 - y^2)^5}{r_0^{10}}\right) \exp\left(\frac{-|\lambda - z|}{S}\right), \quad (7)$$

Where A is the absorptivity of laser (~0.17), r_0 is the laser beam radius, λ is the thickness of the simulated volume and S is the laser absorption depth. The r_0 value used for gaussian and top hat

beam are 40 μm and 100 μm respectively. The S value in this study is limited to the thickness of powder bed (~50 μm). The usage of volumetric heat source had been shown to provide better estimation of thermal history over surface heat source [26].

The thermophysical properties of Ti34Nb are obtained from commercially available thermodynamics software and are listed in Supplementary Information (SI) Table S1. To account for the Marangoni effect on heat transfer, the K above the liquidus temperature was artificially increased by a factor of 2.

The modelling framework contains elements of the powder and substrate. Above the liquidus temperature, T_m of the powder, it is assumed that the powder and substrate have the same K and ρ. However, below the solidus temperature, T_s, The K and ρ of the powder and substrate have the following relationships.

$$K_{powder} = K_{substrate}(1 - \emptyset)^x \,, \tag{8}$$

$$\rho_{powder} = \rho_{substrate}(1 - \emptyset) \,, \tag{9}$$

Where $\emptyset$ is the porosity of the packed powder bed, which is 0.4 and $x \sim 4$ is an empirically determined exponent [27, 28].

At a temperature intermediate of the solidus and liquidus temperature, K and ρ of the material is estimated as [27]:

$$K = \frac{K_{substrate}(T_m) - K_{powder}(T_s)}{T_m - T_s}(T - T_s) + K_{powder}(T_s), \qquad T_s < T < T_m \tag{10}$$

$$\rho = \frac{\rho_{substrate}(T_m) - \rho_{powder}(T_s)}{T_m - T_s}(T - T_s) + \rho_{powder}(T_s), \qquad T_s < T < T_m \tag{11}$$

As the powder undergoes a solid to liquid transformation, upon cooling, it is treated as the solid substrate material.

The latent heat of fusion, ΔH, is incorporated in the modified expression for determining c_p, which is,

$$c_p = \frac{1}{\rho}\left[\theta\rho_{solid}C_{p,solid} + (1-\theta)\rho_{liquid}c_{p,liquid} + \Delta H\frac{\delta}{\delta T}\left(\frac{(1-\theta)\rho_{liquid} - \theta\rho_{solid}}{2\left[\theta\rho_{solid} + (1-\theta)\rho_{liquid}\right]}\right)\right], \quad (12)$$

Where θ is the volume fraction of the solid phase.

2.5. Mechanical Characterization

Two sets of custom designed mini tensile coupons were produced from the LPBF manufactured 350W and 950W Ti34Nb samples using electrical discharge machining (EDM). The two samples and machined tensile coupons are shown in Figure 3a and b, respectively. Reference axes are also indicated in the figure. A schematic of the tensile coupon showing its dimensions is displayed in Figure 3c. Uniaxial tensile test were performed on a universal testing machine (AG-X plus 10 kN, Shimadzu, Japan) with a loading rate of 0.024 mm/min. The tensile coupon is loaded perpendicular to the build direction (y axis in Figure 3b) and the strain is measured with a video extensometer during test (TRview x55s, Shimadzu, Japan). While it is important to conduct tests along the build direction such samples could not be designed due to build volume limitations of our printing setup and the unavailability of powder.

A minimum of three tests were performed for each sample. Fractography was performed with a field emission scanning electron microscope (FESEM) in the secondary electron (SE) mode. Post facto electron back scatter diffraction (EBSD) and back scattered electron (BSE) analysis were performed on the side surfaces (x-y plane) of the coupon.

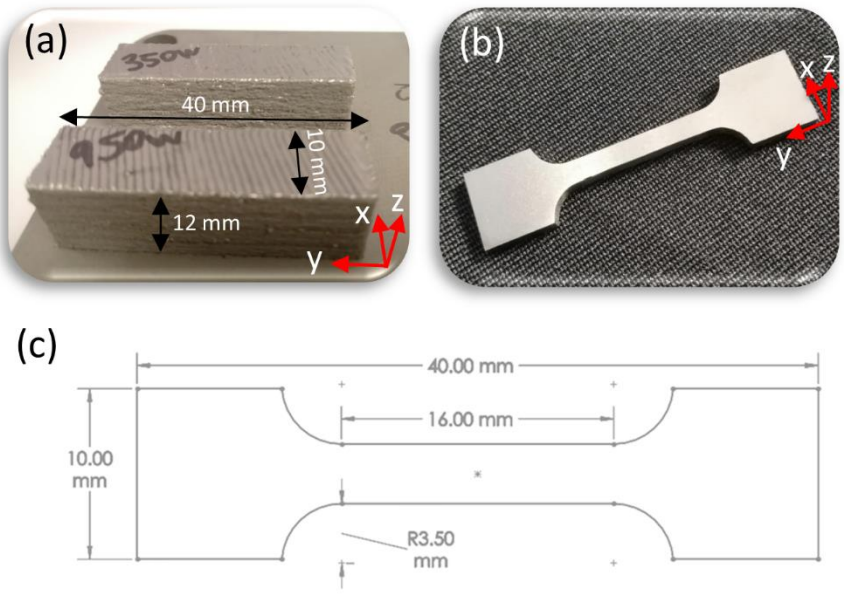

Figure 3 Images of (a) In-situ alloyed parts built via LPBF, and (b) Machined customized tensile coupon. (c) Schematic representation of the customized tensile coupon.

3. Results

3.1. Sample Quality

In-situ alloyed samples printed by LPBF typically contain pores and unmelted metal particles as inclusions. Therefore, the print quality is benchmarked with respect to the porosity and inclusion content. The OM images and 3D reconstructed volumes (obtained from XCT) of the 350W, 650W and 950W TiNb alloy samples are displayed in Figure 4. Pores and unmelted Nb inclusions were identified and colour coded with green and red, respectively, for visualization purposes. The same are also labelled in the corresponding OM images. 3D reconstructed volume from XCT of each sample was analysed with XCT analysis tool and the % volume fraction of porosity, U_P, was obtained. Similarly, the volume % of unmelted Nb inclusions and their median volume equivalent diameter, D_{50}, were also measured. Then, the % unmelted Nb, U_{Nb}, was calculated from the following equation:

$$U_{Nb}(\%) = \frac{\text{Volume \% of Nb particle detected by XCT in sample (\%)}}{\text{Volume \% of elemental Nb particles in powder mix (\%)}}, \quad (13)$$

Where the volume % of elemental Nb particles in powder mix is 21.3%. Note that the XCT analysis can only resolve porosities and inclusions that are larger than a minimum volume equivalent diameter of 14.7 µm. Table 2 lists U_P, U_{Nb}, D_{50} and the density[1] of each sample. In the 350W sample, U_{Nb} ~0.028%, but is 5 times lower in the 650W sample and further reduces to ~0.002% in the 950W sample. Variations in D_{50} also follows a similar trend i.e. it is 43.6 µm in the 350W sample but 37.8 µm and 35.8 µm in the 650W and 950W samples, respectively. Visual examination of OM images in Figure 4 also validates these observations. This indicates that higher laser power assists in-situ alloying by facilitating better melting and mixing of Nb particles, which in turn improves compositional homogeneity of the alloy. This trend in the reduction of the inclusion size is similar to that seen in a study on in-situ alloyed electron beam melted TiNb where lower inclusion size was correlated to increased alloy homogeneity [29]. The Ψ distribution of Nb inclusions are shown in Figure S1 in SI. For all samples Ψ is in the range of 0.8 - 0.9, which confirms that they are predominantly spherical.

Similarly, while U_P ~0.12% for the 350W sample, no pores were observed in the 650W and 950W samples via XCT. The pores in the 350W sample (see Figure S2 in SI) have irregular shapes with well-defined rims and their appearance matches those of keyhole induced porosities [30]. Careful SEM imaging of 650W and 950W samples confirmed the absence of fusion porosity and keyhole induced porosity. However, both samples contain negligible amounts of spherical gas porosities, which have a diameter > 7 µm. Less than 8 pores were detected over an area of 20 mm*15 mm for all samples. Representative SEM images of the

[1] The density should not be directly correlated with the volume fraction of porosity in this study as macro-segregation of unmelted Nb occurs

different types of pores observed in this study are shown in Figure S2 (SI), while the Ψ distribution of the pores in 350W sample is shown in Figure S3 (SI).

Prior studies on LPBF printed TiNb alloys, observed that builds with lower U_{Nb} have a higher content of keyhole porosities and vice versa [20, 21]. *Therefore, the simultaneous reduction in inclusion content and porosity in 650W and 950W samples is a significant breakthrough in process optimization of in-situ alloying with LPBF*. The negligible porosity level also implies that the practice of including an additional remelting/rescanning step for porosity minimization can be discontinued, which will reduce the time and cost of manufacturing [15, 22]. From these results it is evident that printing a 950W laser with a top-hat profile and stripe scanning strategy is most preferable in terms of build quality, time efficiency and cost savings.

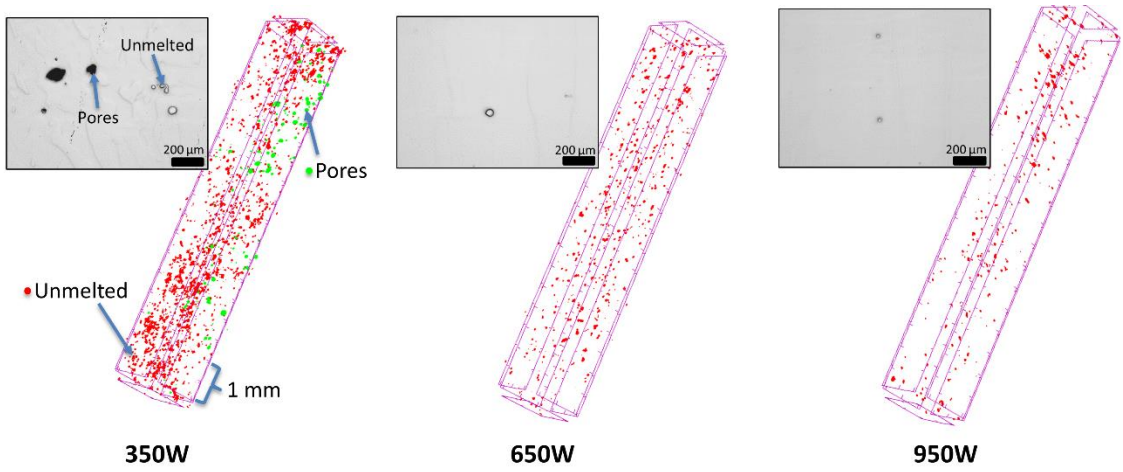

Figure 4. X-ray micro CT reconstruction showing the three dimensional porosity and unmelted Nb distribution in the 350W, 650W and 950W samples. Pores and unmelted Nb are marked in green and red, respectively. Optical microscopy (OM) images of the corresponding samples show the two dimensional appearance of these defects.

Table 2 Summary of the defect characteristics and Archimedian density of the three LPBF printed samples. All values are quoted with a confidence interval of 99.7%..

Sample name	**350W**	**650W**	**950W**
Porosity volume fraction (%), U_P	0.12+-0.1	N/A	N/A
Unmelted Nb (%), U_{Nb}	0.028+-0.0024	0.006+-0.0005	0.002+-0.0002

Median size of unmelted Nb, D_{50} (µm)	43.6+-0.9	37.8+-0.4	35.8+-0.6
Density (g mm^{-3})	5.33+-0.008	5.36+-0.006	5.35+-0.002

3.2. Phase Constituents and Microstructure

EDS and XRD data were examined to evaluate the phase compositions and their respective constituents in the 3 samples and the results are displayed in Figure 5a and b, respectively. In all samples, EDS was performed at locations away from the unmelted Nb inclusions. The Nb content in all samples are ~34% and are within ±1% of the target or expected composition. This is denoted by a dotted horizontal line in Figure 5a. A definitive trend in compositional variations cannot be identified as the scatter will be affected by the resolution limit of EDS. On indexing the XRD scans from each sample, only peaks corresponding to a bcc phase were detected, which indicates the presence of β-Ti in all of them. According to the phase diagram of Ti, the room temperature phase is the α phase that has a hcp crystal structure. Alternately, the β phase is stable above the β transus, which is 700 ^{o}C. However, if the composition of the alloy and cooling rate is suitably adjusted, β-Ti can also be stabilized at lower temperatures. For TiNb alloys the ideal composition for ensuring β stability at ambient temperatures is determined from the Molybdenum equivalency (Mo_{eq}), which is defined as [31]:

$$Mo_{eq}\ (\%) = 1.0\text{Mo} + 0.67\text{V} + 0.44\text{W} + 0.28\text{Nb} + 0.22\text{Ta} + 1.0\text{Al}\ (\text{wt}\ \%), \quad (14)$$

For alloys in the current study, Mo_{eq} ~9.52%, which is very close to the prescribed critical value of 10% required for β stabilization [32]. The retention of β phase at room temperature is further facilitated by the inherent fast cooling rates associated with the LPBF process. A similar result was obtained in a previous study on *in-situ* alloying of Ti35Nb via LPBF [33], although the XRD peaks corresponding to the β phase in this study are comparatively sharper owing to better compositional homogeneity of our samples.

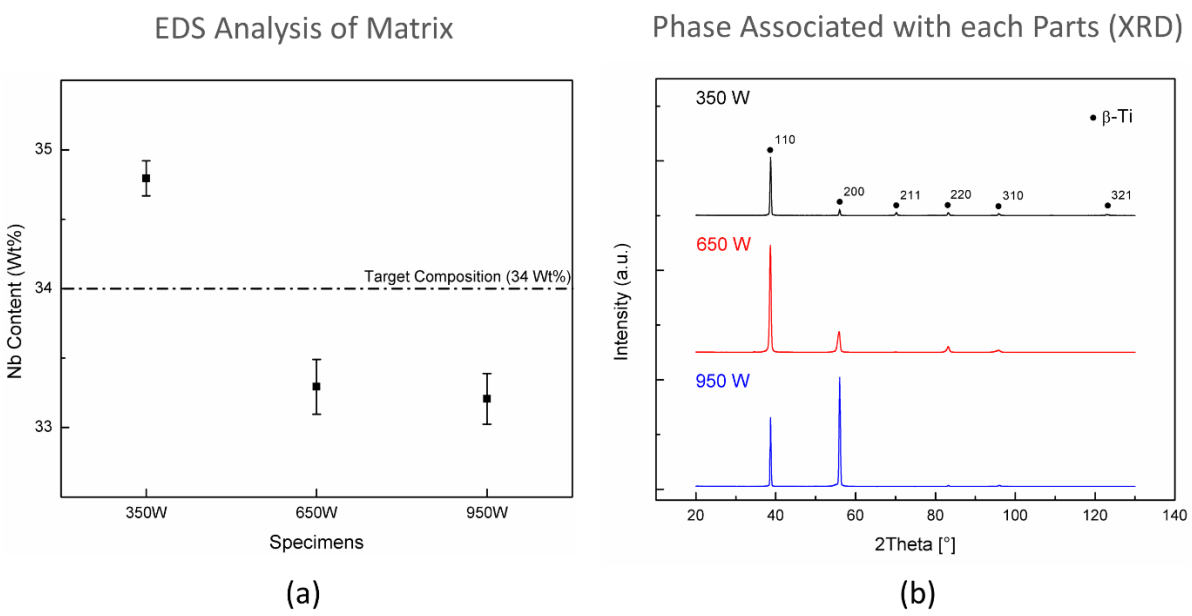

Figure 5 (a) Composition of the three LPBF printed TiNb samples analysed by EDS and (b) their XRD patterns. The error bars represent confidence interval of 99.7%.

Figure 6a displays the SEM images of top view (x-y cross-section) and side view (x-z cross-section) of 350W, 650W and 950W samples. Specific regions of interest in Figure 6a, which are enclosed by blue, red and yellow rectangles are magnified and shown in Figure 6b-d. In the side view of the 350W sample, the melt pools, traced by dashed blue lines, have a relatively high aspect ratio and contain pores within them. The formation of pores within a melt pool of comparatively high aspect ratio provides further evidence that they are keyhole porosities.

The magnified view of a section from the top view of 350W sample (see Figure 6b) reveals that defects such as pores and unmelted Nb are located near the edge of a scan stripe boundary. Although it is relatively less obvious in 650W and 950W samples, the unmelted Nb inclusions in them are also located near the scan stripe boundary (see Figure 6d). The formation of keyhole pores at the scan stripe boundaries of all samples is the outcome of the deceleration or the shutting down of the laser beam at the end of the laser scan [34]. A rapid transition in the laser speed causes vapour collapse followed by partial infill of liquid metal, thereby trapping gas, which in turn leads to pore formation. While this mechanism explains the formation of pores

in the 350W sample, the negligible porosity level in the 650W and 950W samples appears to be an outcome of other factors, which will be addressed later.

Alternately, the formation of un-melted Nb inclusions at the stripe boundaries is an outcome of fast cooling rates, which limits Nb diffusion away from the stripe edge. Fast cooling rates in the vicinity of the scan stripe boundary is facilitated by the rapid heat dissipation to the adjacent solidified stripes and the cold unscanned powder, the two of which act as heat sinks. In addition, the extent of re-melting near the stripe boundaries is limited, which further contributes to the amount of un-melted Nb inclusions.

A magnified view of the stripe centre region in 350W samples is shown in Figure 6c. This region has a coarser cellular substructure compared to that in the stripe boundary region, indicating that it experienced a relatively slower cooling rate [35]. Moreover, the grain growth direction in the stripe boundary region, near unmelted Nb, is relatively random (see Figure 6b and Figure 6d), unlike that in the stripe centre region (Figure 6c), where grains grow along the BD.

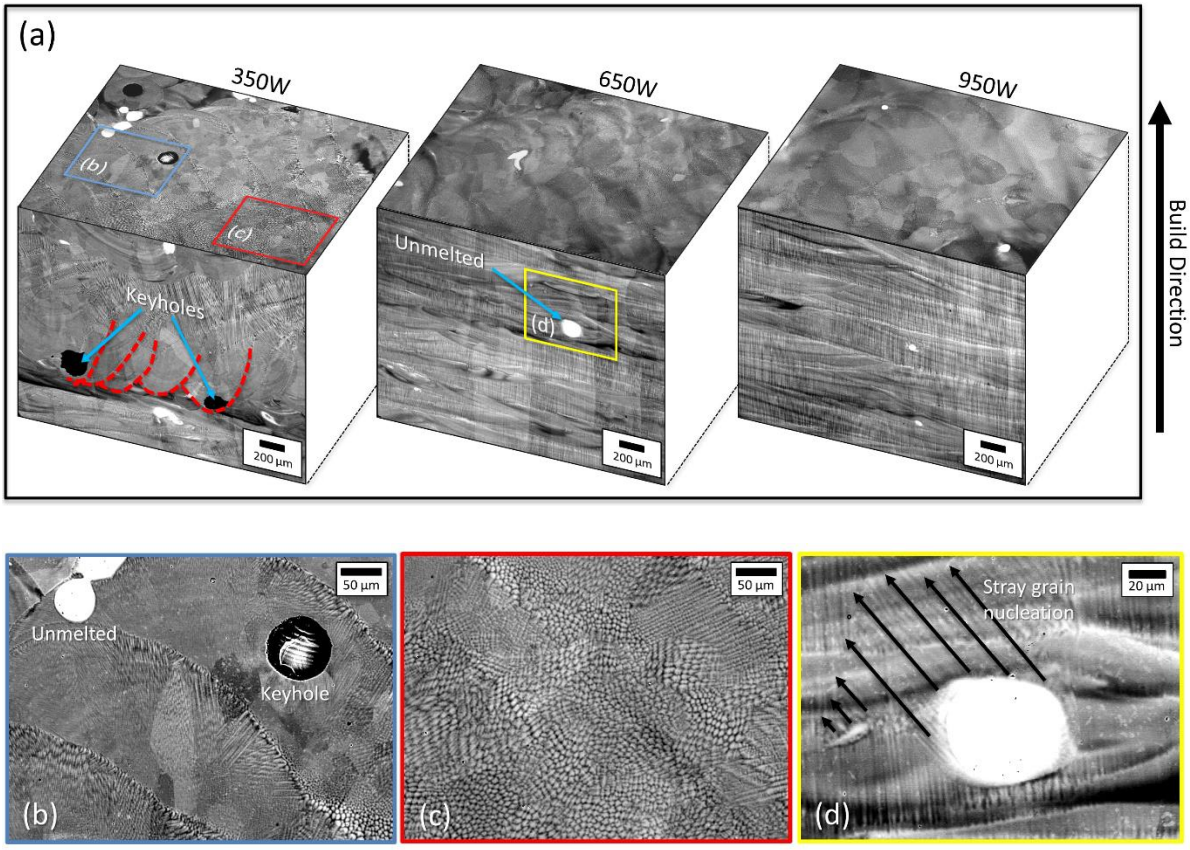

Figure 6 (a) 3D representative microstructures of 350W, 650W and 950W samples imaged in the BSE mode. Microstructures of the 350W samples (b) near the end of laser scan track, and (c) middle of laser scan track. d) High magnification BSE image of unmelted Nb in the 650W that is enclosed within a yellow rectangle in (a). Dashed lines in (a) are used as guides to show the melt pool boundary.

The (100) pole figures, which are the graphical representation of the textures, of 350W, 650W and 950W samples are displayed in Figure 7a-c, respectively. All samples have the {100} fiber texture, which implies that the {100} direction of most grains are oriented along BD whereas other crystallographic directions have random orientations. Fiber texture is typically associated with directional grain growth, which leads to the formation of columnar grains. The multiple-of-uniform-density (MUD) value, which is also referred to as the 'texture strength' and describes the relative strength of a particular orientation in the sample w.r.t. other orientations, is calculated for {100} and is presented in each pole figure. MUD for 350W is 19.51 but is 42.38 and 52.02 for 650W and 950W samples, respectively.

Figure 8a-c shows the grain orientation maps of 350W, 650W and 950W samples, respectively, on the y-z cross section with inverse pole figure Z (IPF-Z) colouring. In all samples, the

majority of the β-Ti grains are elongated and colored in red, confirming that the microstructures predominantly consist of columnar grains with their {100} crystallographic directions oriented parallel to the BD. However, the 350W sample also contains a significant fraction of randomly oriented smaller grains. Such randomly oriented grains are much lesser in 650W and 950W samples. This is consistent with the above-mentioned trend in the strength of fiber texture for the three samples.

Next, the grain widths in each sample is measured and its distribution is shown in Figure 9. The average grain width of the 350W sample is 71 μm, whereas that of the 650W sample is 160 μm. 950W sample has the largest average grain width of 243 μm, which suggests that grain coarsening occurs with progressive increase in the scanning laser power. Then, the proportions of high angle grain boundaries (HAGBs) and low angle grain boundaries (LAGBs), which are defined for grain boundary misorientations, $\kappa > 15^o$ and $2^o < \kappa < 15^o$, respectively, were also measured. The percentage of LAGBs in the 350W sample is only 25% whereas in the 950W sample it is almost 60%.

On analysing the grain orientation map of 950W sample (see Figure 8c) further, it was noted that almost all stray grains contain an unmelted Nb inclusion at the bottom, which are marked by white arrows. Similar observations were made in 650W and 350W samples as well (not marked in the images to preserve clarity). This suggests that stray grains prefer to nucleate near unmelted Nb inclusions and since 350W samples have high U_{Nb}, a relatively higher proportion of stray grains are present in them. Alternately, samples 950W and 650W, which have lower U_{Nb}, exhibit greater grain widening.

From these results, it is evident that a predominantly columnar microstructure with a strong {100} fiber texture and high average grain width can be obtained by implementing the printing parameters corresponding to the 650W and 950W sample.

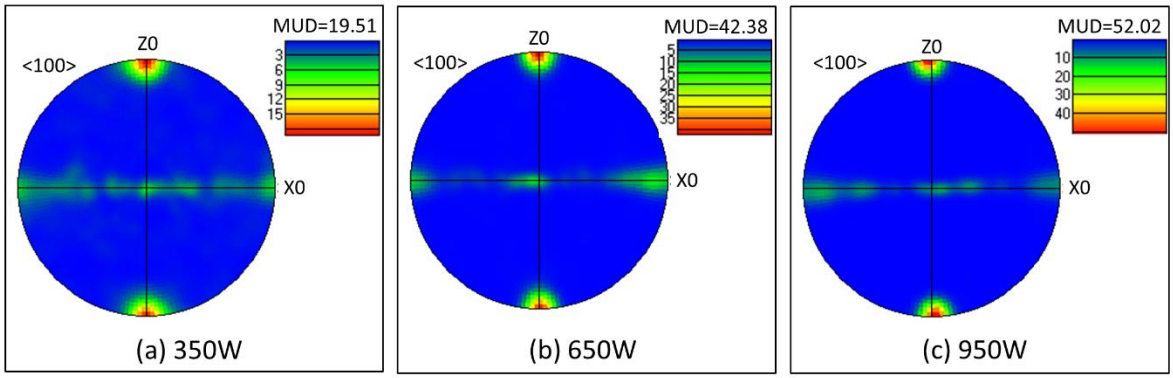

Figure 7 Texture distribution represented by the (100) pole figure for (a) 350W (b) 650W, and (c) 950W samples.

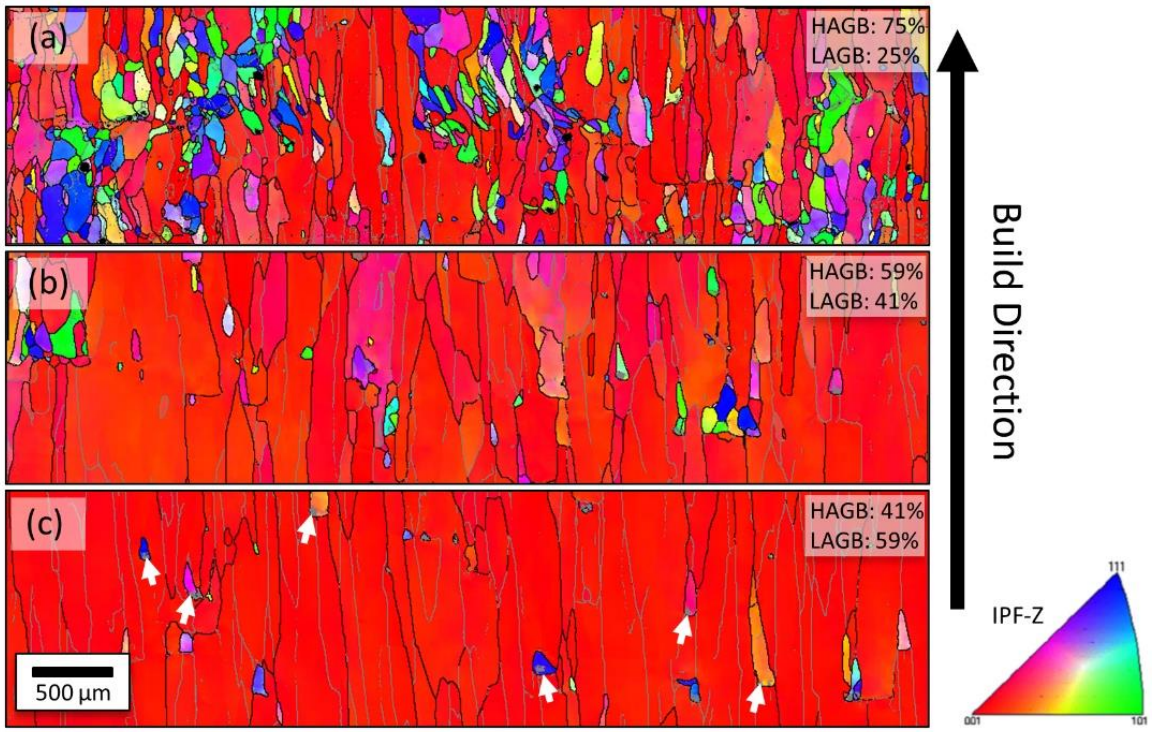

Figure 8 Representative grain orientation maps (IPF-Z colouring), obtained using electron back scattered diffraction (EBSD) for (a) 350W (b) 650W and, (c) 950W samples. (d) Pole figure for 350W. LAGB (2º – 15º) are depicted with gray while HAGB (> 15º) with black lines. The white arrows in (c) indicate the presence of un-melted Nb inclusions.

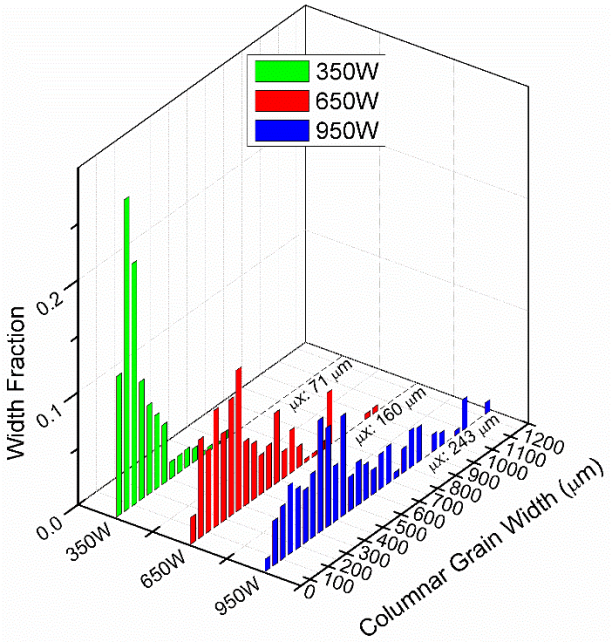

Figure 9 Grain width (short axis of columnar grain) distrbution of the as-printed samples.

3.3. Melt Pool Morphology

The melt pools formed in single stripes were examined with SEM to understand the underlying differences in melt pool formation. Figure 10a-c are SEM images of the cross-sections of single stripe (cross section perpendicular to the direction of single track scans at the top layer) of 350W, 650W and 950W samples, respectively. The single stripe of the 350W sample has the shallowest melt pool depth, d of ~122 μm, while d ~200 μm and 181 μm for those of 650W and 950W samples, respectively (see Figure 10a-c). Variations of d among single stripes are unlike what was seen in single tracks (Figure S4 in SI), in which the details can be found in SI. Interestingly, the maximum slope of melt pool boundary, θ, which is measured at the intersection between the melt track profile and re-melt layer (shown in Figure 10a-c), is smaller for deeper melt pools. The slope of the melt pool boundary, θ, in the 350W sample is 28^o, whereas it is 15^o and 16^o for the 650W and 950W samples, respectively.

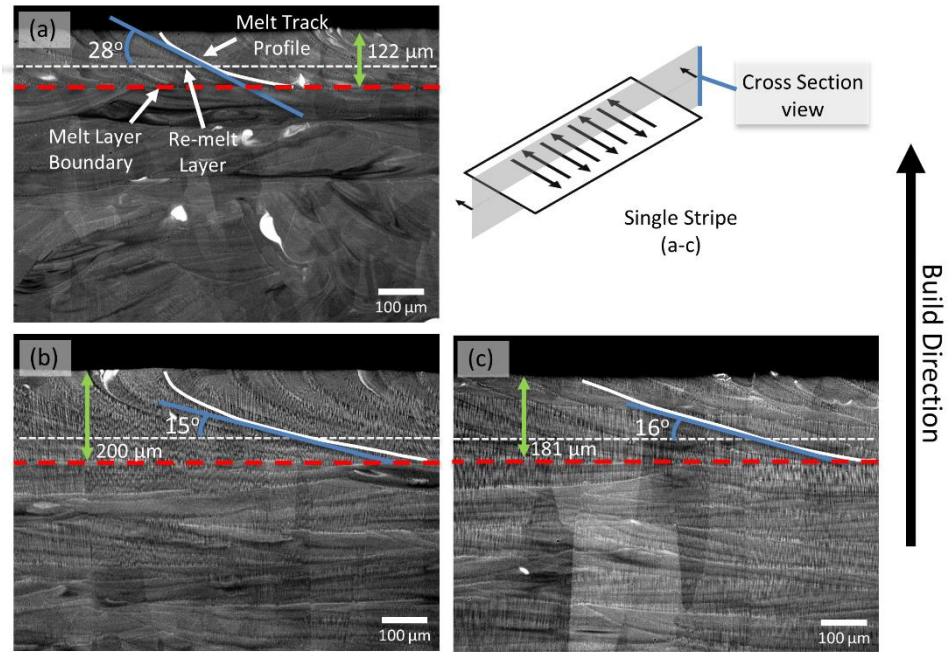

Figure 10. Representative SEM images of single stripes (top layer, cross section view) corresponding to (a) 350W, (b) 650W, and (c) 950W samples. The maximum angle of melt pool boundaries are measured as the angle tangential to the melt track profile at the intersection between melt track profile and the re-melt layer.

The top surfaces of the single stripes are further examined to determine other features of the corresponding melt pools. Figure 11 shows the surface topology of the single stripe scans corresponding to 350W, 650W and 950W samples. The laser scanning directions are indicated by black arrows and superimposed on the scans. Several curved lines, appear on top of all the as-built parts, which are identified as solidified traces of ripples that form on the melt pool during laser scanning [36]. These ripples, marked with black lines on the images, are analogous to those formed on water surfaces from an external disturbance [37]. They travel radially outward from the source of disturbance, which is the laser heat source, and terminate at the edge of the melt pool boundary. At the edge of the melt pool boundary, the ripples conform to the melt pool boundary curvature and solidify when they reach the melt pool boundary. Consequently their shape and widths can be approximately equated with that of the melt pool boundary. In the 350W sample, the ripples have two distinct portions with different curvatures, one perpendicular to the laser scanning path and the other parallel to it. The portion perpendicular to the scanning path has a smaller span (~200 µm) and radius of curvature

compared to that of the latter, which implies that the melt pool boundary is elongated along the direction of the laser scanning path. In contrast, the ripples in 650W and 950W samples span > 1 mm and have a large but uniform radius of curvature along its length. This implies that the melt pool in these samples are significantly larger with roughly semi-circular boundaries. Moreover, these ripples' characteristics also hinted the direction of meltpool velocity, which is along the laser scanning direction for 350W but perpendicular to the laser scanning direction for 650W and 950W. Equating the ripple span with that of the melt pool width, w, it is determined that 350W samples have the melt pool aspect ratio, $d/w \sim 0.61$, whereas those of 650W and 950W samples is 0.2 and 0.18 respectively.

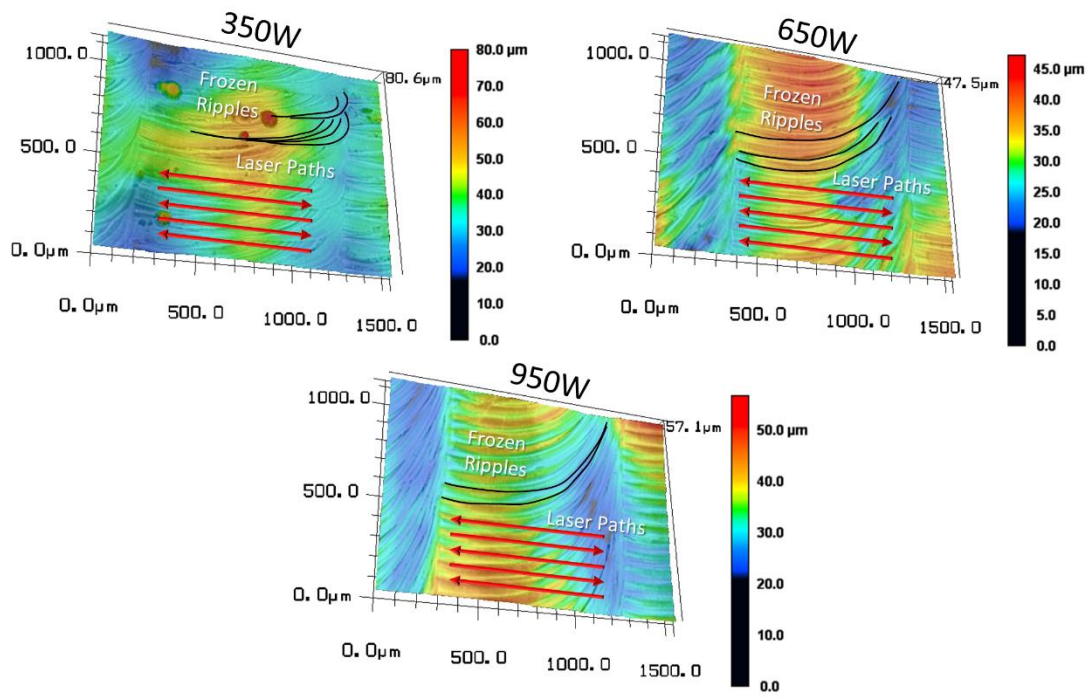

Figure 11 A confocal microscopy scan showing the topology of the top surfaces for (a) 350W (b) 650W and (c) 950W samples. The red arrows illustrate the stripe scanning path of laser (not to be scaled and meant for illustration purposes only). The black lines highlights several frozen ripples within a single stripe scan.

3.4. Thermal analysis of melt-pool

To understand differences in the evolution of single stripe melt pools in 350W and 950W samples, their corresponding thermal profiles were simulated by thermal FEM. The simulated

melt pool morphologies of the 350W and 950W samples, after the stripe scans achieve a steady state, are shown in Figure 12a and b. Based on the color coding of thermal intensity, the positions of the laser source and the melt pool were identified. For the 350W sample, a small melt pool can be seen growing along the direction of the laser scan (see Movie S1 in SI). This melt pool solidifies shortly after the laser scan moves ahead and since it does not interact with the adjacent linear laser scan, the melt pool velocity, $V_{m,350}$, can be approximated to be the same as the laser scanning velocity, $V_{L,350}$.

In contrast, a huge melt pool, whose width is a multiple of the stripe width, forms in the 950W sample (see Figure 12b). Such a melt pool is the manifestation of interactions between multiple laser passes of constant hatch spacing. Simulations also indicate that due to the high speed and power of the laser employed, the melt pool induced by the first scan is unable to solidify completely and interacts with the melt pool created by the adjacent scan (see Movie S2 in SI). Besides creating an additional melt pool in its location, the adjacent scan provides energy input to the existing melt pool and prevents its solidification. This results in the merger of several melt pools, resulting in a single large melt pool that spans multiple stripe widths. Moreover, the large melt pool grows and traverses perpendicular to the linear laser scan direction (see Figure 12b and movie S2 in SI). Hence, the meltpool velocity of the 950W sample, $V_{m,950}$, can be rewritten as:

$$V_{m,950} = V_{L,950} \cdot \frac{H}{S}, \tag{15}$$

Where H is the hatch spacing and S is the stripe width. The experimental observation of ripples formation (Figure 11) well agrees with the simulated melt pool traverse direction. This unique type of melt pool dynamics, which results from the interaction between adjacent scan tracks, was also observed by Sun et al. in 316L stainless steel when they used an appropriate combination of high P and V_L and scanning strategy [38].

From equation (15), the ratio of melt pool velocity of the 950W and 350W samples is expressed as:

$$V_{m,950}/V_{m,350} = V_{L,950}/V_{m,350} \cdot \frac{H}{S}, \quad (16)$$

In this study, $\frac{V_{m,950}}{V_{m,350}} = 0.217$, which implies that the melt pool velocity using the parameter set corresponding to 950W is 4.6 times slower than that of 350W. Figure 12c and 12d are x-z cross sections of melt pools associated with the 350W and 950W samples. These cross sections are taken from Figure 12a and 12b at the locations corresponing to that observed in experiments and displayed in Figure 10a and c. The y-z cross-sections of the same are displayed in Figure 12e and f. In Table 3, the dimensions and characteristics of the meltpool obtained from experiments and simulations are listed and compared. The simulated values of *d* for the 350W and 950W samples are 119 μm and 180 μm respectively, which is very close to that observed in experiments. Moreover, a close match is obtained between the experimental and simulated values of *w*, *d/w*. Note that *w* is measured in the direction perpendicular to the melt pool motion (see Figure 12a and 12b). However, there is a significant difference in the experimentally measured and simulated values of θ in the 350W sample, which are ~49^o and ~28^o, respectively. This difference is attributed to the understimation of absorptivity in the simulations of the 350W sample. Since significant overlap of meltpools smears out the variance in absorptivity, a similar divergence in the values of θ in the 950W sample is not observed. Nevertheless, the trend in the variations of all parameters in experiments and simulations are consistent for the two samples. The good conformance of dimensional aspects evaluated from simulations and experiments suggests that the melt pool velocities, V_m, determined via simulations are reliable. Based on this premise, it is reasonable to state that the approximate melt pool volumes, determined via simulations and henceforth referred to as $d \times w \times l$, of 350W and 950W samples

would correspond to the actual melt pool volumes. The latter has a $d \times w \times l$ of 0.15 mm^3, which is an order of magnitude higher than that of the former.

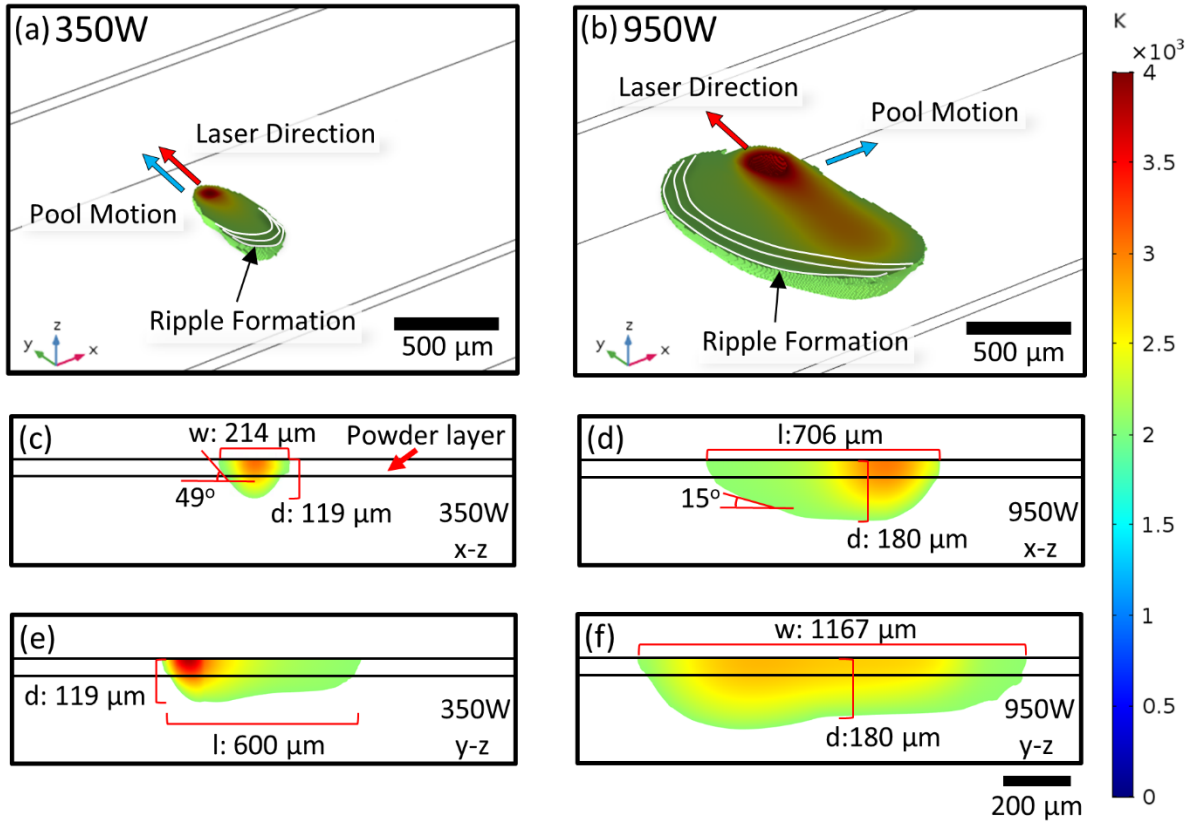

Figure 12 Simulated temperature profile snapshots, which represents the meltpool evolution in a single stripe during laser scanning with printing parameters corresponding to (a) 350W and b) 950W samples. The x-z cross section of the simulated profiles at the locations corresponing to that observed in experiments for parameters corresponding to (c) 350W and (d) 950W samples. y-z cross sections of the same location for (e) 350W and (f) 950W samples. The 200 µm scale bar is applicable for figure c - f.

Table 3 Dimensions and characteristics of the melt pool obtained from experiments and simulations.

Melt Pool Characteristics	**350W**		**950W**	
	Experiment	Simulation	Experiment	Simulation
***d* (µm)**	122	119	181	180
***w* (µm)**	~200	214	~1000	1167
***l* (µm)**	N/A	600	N/A	706
d/w	0.61	0.56	0.18	0.15
***θ* (°)**	28	49	16	15
***d*×*w*×*l* (mm^3)**	N/A	0.015	N/A	0.15

*experimental melt pool width estimated from ripple observation

3.5. Tensile Properties

To assess which microstructure vis-à-vis the printing parameters, leads to superior mechanical properties, tensile tests were performed on the coupons obtained from 350W and 950W samples.

Their representative engineering stress, σ, vs. engineering strain, ε, responses are shown in Figure 13. In the inset, the measured values of Young's modulus, *E*, yield strength (YS), ultimate tensile strength (UTS), and strain to failure, ε_f, for the two samples are also displayed. The 350W sample has *E* which is 14% higher than that of 950W sample. This difference is expected because although the two samples have similar textures, the former has a higher proportion of stray grains, whose *E* are expected to be slightly higher [39]. The 350W has higher YS due to its comparatively finer grain structure, which leads to greater Hall-Petch strengthening. However, beyond the yield point, the two samples undergo strain softening and exhibit nearly perfectly plastic stress-strain response until failure. Also, the ε_f of the 350W and 950W samples are comparitively lower than those of conventionally manufactured TiNb alloys, which have ε_f >8% [40].

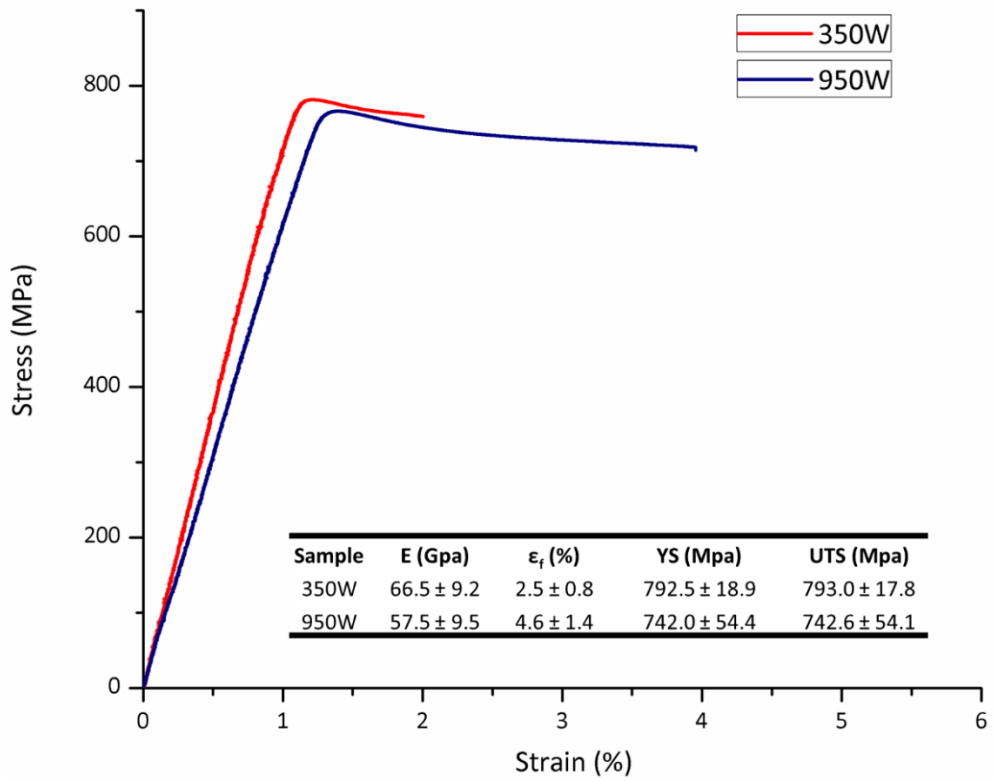

Figure 13 Tensile stress-strain response of of 350W and 950W samples. All values are quoted with confidence interval of 99.7%..

To understand the lack of strain hardening and origin of low ductility of these alloys, post-facto microstructural analysis and fractography were conducted on the tensile-tested samples. The side surfaces of the samples were polished and examined under the SEM. Figure 14a and b display the EBSD band contrast images of these side surfaces for the 350W and 950W samples, respectively. Some of these twins and slip bands are also identified in BSE image of the unetched 950W sample, as indicated in Figure 14c. While traces of slip bands were observed within all grains (marked with yellow arrows in Figure 14a-c), a few twins were also observed in some grains, which was mapped by EBSD and superimposed over the band contrast images of the two samples. Figure 14d displays the relative fraction of misorientation angles of the twins present in 350W and 950W samples. In the 350W sample, only the {112}<111> twin system was indexed whereas the two {112}<111> and {332}<113> twin systems were indexed

in the 950W sample. Since the EBSD mapping was done on highly deformed and distorted areas near the fracture surface, some twin boundaries were not captured. Nevertheless, the two samples are expected to contain the same twin systems as they are compositionally alike. In Figure 14e and f, the fracture surfaces of the tensile-tested 350W and 950W samples are displayed. The two samples exhibit a mix of intergranular and transgranular brittle fracture features. Fracture along the keyhole induced porosity can be also be observed on the fracture surface of 350W. In contrast, the fracture surface of the 950W sample shows stepped cleavage facets with self-similar cleavage angles, which is characteristic of failure occuring in columnar grains. Based on these results, the following is a description of the deformation mechanisms in the LPBF manufactured TiNb samples:

On yielding, deformation occurs via planar slip of dislocations on either of {110}, {112} or {123} planes, which leads to the formation of several slip bands. Negligible interactions between dislocations during planar slip leads to localization, which manifests as strain softening in the stress-strain curve. A similar lack of strain hardening was also observed in other metastable β-Ti alloys undergoing planar slip during plastic deformation [41, 42]. At a later stage of deformation, twins form in the two samples, which could reorient the crystal to potentially facilitate slip on multiple planes and lead to interaction between dislocations. However, since no change in the strain softening behavior of the two samples is observed with continued straining, these twins appear to have an insignificant effect on the overall deformation response. One reason for this could be that the volume fraction of twins is lesser than that required for interfering with slip in the material. This argument is supported by the fact that even at the point of failure, only few twins were observed in isolated grains, whereas almost all grains contained a dense array of slip bands. Despite similar deformation mechanisms, the 950W sample has higher ε_f than the 350W sample. This could be attributed to the presence of keyhole pores in the latter that serve as stress concentrators and lead to

premature failure. Overall, while the 950W sample is superior than 350W sample in terms of E and ε_f, the latter is marginally stronger. Nevertheless, the two alloys exhibit strain softening and undergo strain localization during plastic deformation.

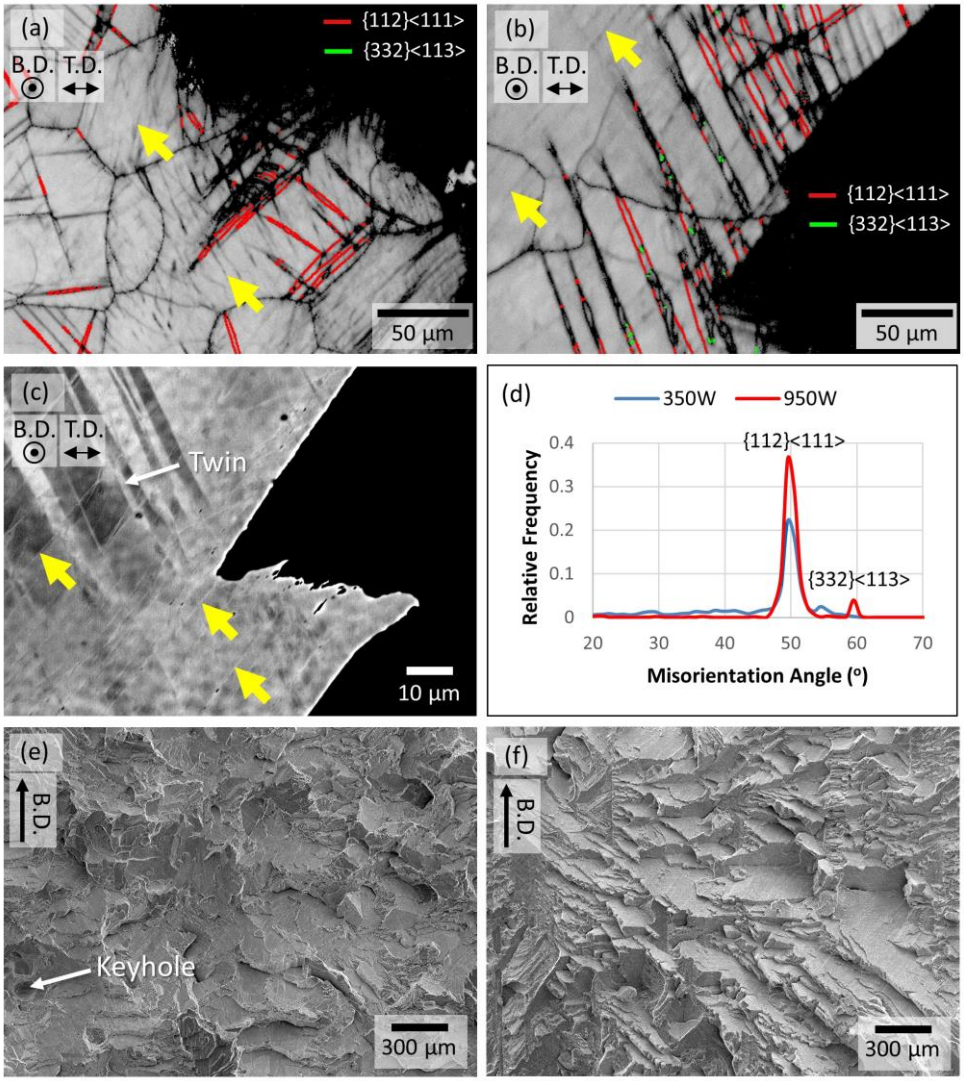

Figure 14 Post facto EBSD mapping of the side surfaces of tensile-tested (a) 350W and (b) 950W samples showing twin boundaries overlaid on band contrast. (c) Post facto BSE micrograph of the side surface of tensile-tested 950W sample. (d) Misorientation angle distribution from EBSD analysis in (a) and (b). The representative fracture surface of (e) 350W and (f) 950W sample.The yellow arrows are used to indicate the slip band traces. The BD and tensile direction (TD) are indicated wherever applicable.

4. Discussion

4.1. Mechanisms of microstructure formation

Melt pool solidification in all samples initiates by columnar grain growth along the build direction, as it coincides with the direction of the maximum thermal gradient. In the 350W sample, although the microstructure is predominantly composed of columnar grains, the formation of several stray grains is also observed. The other two samples also contain similar stray grains, albeit in significantly lower proportions. The formation mechanism of these stray grains has been a topic of debate in studies where *in-situ* alloyed β-Ti with Nb or Ta were produced via LPBF. Some studies on Ti-37Nb-6Sn (wt%) and Ti-26Nb (at%) correlate the stronger {100} texture in the BD with increasing E_d input but do not explain how the texture evolved [20, 21]. Sing et. al observed that the stray grains in their Ti-50Ta are an outcome of the columnar-to-equiaxed grain transition (CET) in the alloy, which depends on the relative magnitudes of the thermal gradient and dendritic growth rate at a location [43]. In contrast, Brodie et. al [22] and Huang et. al [44] suggest that heterogeneous nucleation of grains from unmelted Ta or Nb particles or processes involving constitutive undercooling of the melt near the Ta particle lead to the formation of stray grains in Ti-Ta alloys. Although our observation that unmelted Nb inclusions exist beneath a stray grain supports the arguments of Brodie et al. and Huang et al., we nevertheless examine the variations in thermal gradient, G and dendrite growth rate, R, for the 950W and 350W samples to assess if CET can occur in the absence of inoculants. For this, the primary assumption is that the alloy system is assumed to be homogenous and that grain nucleation does not occur on un-melted Nb particles. Then, the Kurz-Giovanola-Trivedi (KGT) model [45] was used to obtain the relationship between the undercooling temperature, ΔT_c and R. Then, the Hunt's criterion for growth of equiaxed grain is applied to obtain a relationship between G and ΔT_c [46]:

$$G = 0.6N_o^{\frac{1}{3}}\Delta T_c\left(1 - \frac{\Delta T_n^3}{\Delta T_c^3}\right), \quad (17)$$

Where G is the thermal gradient, N_o is the density of heterogeneous nucleation sites for equiaxed grains and ΔT_n is the nucleation temperature.

ΔT_c was replaced with R in Eq. (17) and the parameters used for applying the KGT model and Hunt's criteria were obtained from Ref. [47], which were suitably modified for the current alloy composition. Figure 15 shows the plot of R as a function of G, which is referred to as the CET curve, and is utilized for identifying specific regimes corresponding to columnar and equiaxed growth. As equiaxed grain growth is favoured when $G < R$, i.e. the region to the left of the curve corresponds to the equiaxed grain growth regime. Using the thermal history data from FEM, the values of G and R in the melt pool within the mushy zone is evaluated and superimposed on the plot (see Figure 15), to examine the grain growth behaviour of 350W and 950W samples. Data points corresponding to the two samples lie in the columnar grain growth regime, which rules out the formation of equiaxed grains at any stage of solidification. The alternate mechanism of stray grain growth is schematically illustrated in Figure 16. As the laser beam scans the powder bed, a melt pool forms and then solidifies to form columnar grains, which grow epitaxially over the previously printed layer. It is also easy to visualize that epitaxial growth of {100} grains in the build direction would be favoured when θ is gentler, as seen in 950W samples. If the melt-pool contains unmelted Nb, grain growth can occur in its vicinity via either of the following mechanisms. The first mechanism suggests that during solidification, Nb diffuses into the melt and creates conditions of constitutional supercooling in its vicinity, which leads to the spontaneous formation of several nuclei. These nuclei grow into grains with random orientations. If this were the operative mechanism, the 950W sample, which facilitates maximum diffusion of Nb in its melt pool, would exhibit a greater extent of constitutional supercooling and should contain a larger number of stray grains than the 350W

sample. The alternate mechanism suggests that Nb is an inoculant and acts as a heterogeneous nucleation site for the formation of short columnar grains, along directions that satisfy the appropriate orientation relationship. In this scenario, there would only be a few stray grains in the vicinity of a Nb inclusion. Since our experimental results show that 950W samples have only 1 or 2 such grains near a Nb inclusions (see Figure 8c), the second mechanism, involving heterogeneous nucleation, is more likely to facilitate stray grain formation.

The solidification mechanism also affects the relative proportions of LAGBs and HAGBs in the TiNb samples. The rapid cooling and thermal gradient in the melt during LPBF generate residual stresses in the solidified material. Repeated heat input from multiple laser scans relieves this residual stress and triggers polygonization, which in turn results in the formation of several LAGBs in the material [48-51]. This mechanism has also been reported for several other Ti alloys where epitaxial growth of columnar grains was observed [21, 52]. However, since stray grains form rapidly from a heterogeneous nucleation source, polygonization does not occur, which leads to the formation of HAGBs around them. Therefore, the 950W sample, which have a lower proportion of stray grains, has a relatively higher proportion of LAGBs whereas the converse is true in the 350W sample.

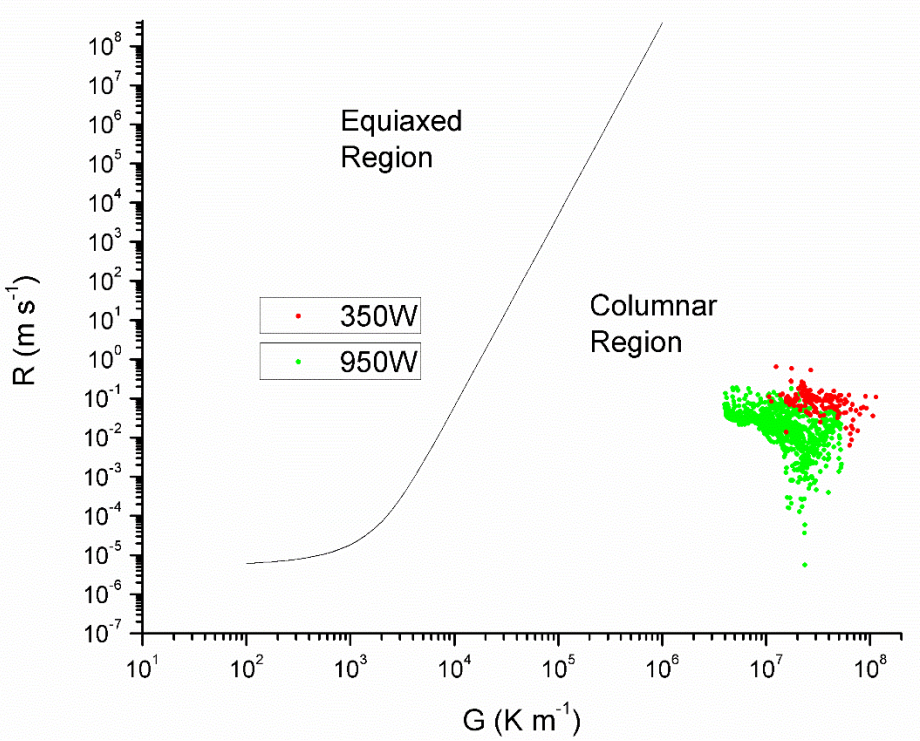

Figure 15 Plot of dendritic growth, R, and the thermal gradient, G, for Ti34Nb. The range of values of G and R in the melt pools of 350W and 950W samples are superimposed on the plot to assess the possibility of columnar to equiaxed transition of grains.

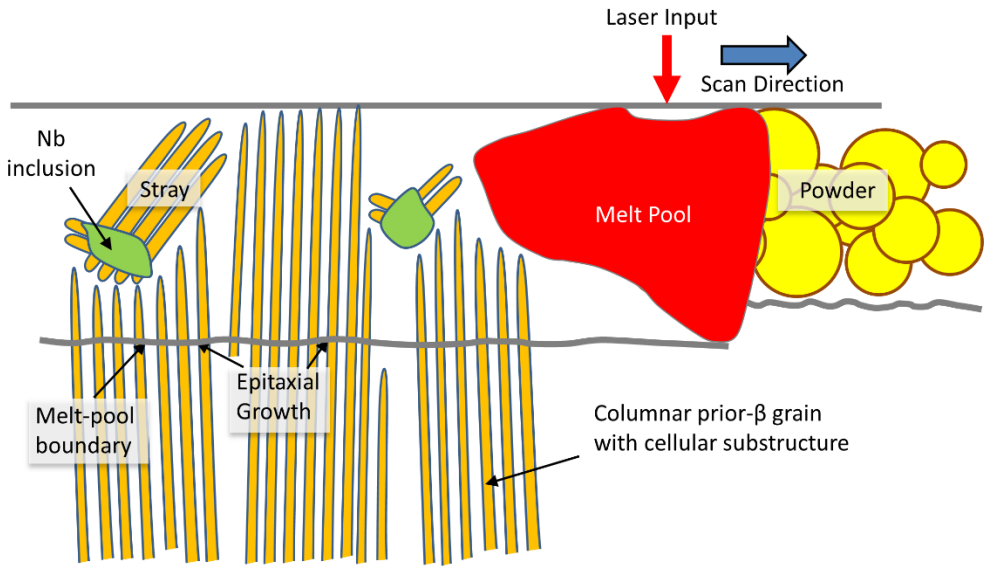

Figure 16 Schematic of stray grain formation due to unmelted Nb particles.

4.2. Melt pool size control by parameter optimization

From the analysis of the melt pool characteristics, it is evident that $d \times w \times l$, V_m, d/w and θ, all influence the quantity of unmelted Nb, keyhole porosity and microstructure in LPBF built TiNb alloys. A combination of large $d \times w \times l$ and low V_m such as that seen in 950W sample, promotes homogenization by preventing localised melting, lowers the rate of cooling in the melt pool and provides enough time for the heat to distribute evenly. Therefore, all the constituents, specifically Nb, has sufficient time for diffusing and mixing before the melt pool solidifies, resulting in lower content of unmelted Nb in the alloy. The slower cooling rate in the meltpool, due to large $d \times w \times l$ and low V_m, is also the primary cause for grain coarsening in the 950W samples. Alternately, lower d/w and V_m of the melt pool ensure that 650W and 950W samples have vanishing keyhole induced porosity, although the exact mechanism for this is still not well understood. Nevertheless, it is reasonable to expect that a low aspect ratio (d/w) melt pool would be less prone to collapsing and forming shut pores [34].

Lower θ aligns the thermal gradient along the build direction, which in turn increases the strength of {100} fiber texture of the columnar β-Ti grains along the build direction. The formation of columnar grains with a dominant {100} texture is also promoted by a large $d \times w \times l$ and low V_m as they suppress unmelted Nb content, which in turn decreases the possibility of strain grain formation. Note that, in terms of lower elastic modulus requirements of implants, the {100} fiber texture is highly preferred. This is because the Young's modulus along the <100>, E_{100} ~ 39.5 GPa, which is at least 1/2 and 1/3rd of that along <110> and <111>, respectively [39]. A dominant {100} texture will ensure that the polycrystalline alloy has the lowest value of E. Note that the preference for obtaining a columnar grain structure in this study is exclusively relevant for developing components such as in hip implants and jet engine turbine blades, which are directionally loaded. Otherwise, in the absence of these application

specific requirements, an equiaxed grain structure is more sought after for its refined grain size and isotropic properties.

From these observations it is evident that a melt pool with a combination of low V_m, low d/w, low θ and large $d \times w \times l$, is ideal for printing pore free TiNb implants that have {100} textured β-Ti columnar grains and minimum unmelted Nb inclusions. As indicated by simulations in section 3.4, a melt pool with these characteristics can be developed by printing with high values of P and V_L. Note that this particular printing recipe is successful only when a sufficiently small stripe width, such as the one mentioned in this work, is employed. If the stripe width is significantly high or approaches the length of a single track, an existing melt pool would solidify before the laser returns to scan the adjacent regions. This would limit interactions between multiple smaller melt pools, which is necessary for obtaining the above-mentioned combination of V_m, d/w, θ and $d \times w \times l$.

Besides these factors, the influence of the laser profile on the melt pool dimensions is also worth examining. We refer to the single-track melt pool dimensions of the 350W and 950W samples, which were printed with Gaussian and top-hat profile lasers, respectively (see section S1, Figure S4a and c in SI). As can be seen in these images, the melt pool of the former is much deeper and narrower than that of the latter, which suggests that the top hat laser profile typically leads to a lower d/w. This is expected because a Gaussian profile has a conical shape and concentrates the laser energy at its apex (see Figure 1a), thus favouring the formation of a melt pool with a high d/w. In contrast, the cylindrical shape of the top hat laser profile distributes the laser energy over the scanned area and facilitates the formation of a melt pool with low d/w. On the basis of the above-mentioned discussions, which suggests that an optimum melt pool should have a lower d/w, the top hat laser profile appears to be more favourable than the Gaussian profile.

However, it may be inappropriate to equate the characteristics of melt pools obtained from single tracks and single stripes as their formation mechanisms are distinctly different. Extending this premise further, it may also be argued that it is possible to obtain the desired melt pool attributes by simply employing the ideal combination of P, V_L and stripe width, regardless of the laser profile. Moreover, there is a possibility that the relatively larger spot size of the top-hat laser, compared to that of the Gaussian laser in this study, may be a more relevant parameter to consider. To address these arguments, we simulated the thermal profiles of single stripes with (a) a Gaussian profile laser and a spot size of 80 μm, (b) a Gaussian profile laser and a spot size of 200 μm profiles and (c) a top-hat profile and a spot size of 80 μm, with all other parameters corresponding to that used for printing the 950W sample. The simulated melt pool geometries of the above-mentioned conditions are shown in Figure S5 (SI). For lasers with spot sizes of 80 μm and 200 μm, the top-hat profile laser yields melt pools with identical V_m, d/w, θ and $d \times w \times l$. Similarly, simulated thermal profiles of melt pools generated by a laser with Gaussian profile, but with different spot sizes, are also identical, which implies that the spot size has no influence on melt pool characteristics or dynamics. Moreover, the simulated melt pool formed by a laser with a top-hat profile is superior to that formed with a Gaussian profile as it possesses the ideal combination of V_m, d/w, θ and $d \times w \times l$ (see also Movie S1 and S2). This confirms that besides P, V_L and stripe width, the choice of a laser profile is also critical for obtaining the ideal melt pool attributes.

While prescribing this particular parameter optimization strategy, we also recognize that three critical questions could be raised. First, is it also possible to eliminate unmelted Nb completely by further increasing P and V_L? Although the limitations of our printing setup prevented us from testing this hypothesis, it is reasonable to expect that further increasing P and V_L, would produce a larger melt pool with a reduced cooling rate. Such a melt pool would promote complete melting of Nb particles but will also promote grain coarsening, due to a slower

cooling rate, and this is undesirable from the mechanical property perspective as coarse-grained materials have lower strengths. Also, the formation of a large melt pool limits the smallest feature size and compromises the dimensional precision of the build. This is because the size of the melt pool is limited by the external dimensions of the build and if the melt pool forms at the latter's edge, the molten material may accidentally overflow or lose shape, which will alter the final dimensions of the build. However, this caveat can be resolved by altering the single stripe width to limit the dimensions of the melt pool according to the feature size.

Second, is the prescribed strategy uniquely applicable for *in-situ* alloying of TiNb using LPBF or can it be adopted for pre-alloyed powder to print highly dense parts of any material? We do not yet know the answer to this question as we did not apply it on different types of pre-alloyed powder. Nevertheless, if the processing parameters required for forming a single stripe melt pool with the optimum dimensions are determined, we hypothesise that it is possible to print any material with negligible porosity. In the broader context, this implies that the next technological advancement towards porosity minimisation in LPBF manufactured materials requires dedicated efforts towards determining the processing window, which optimizes the dimensions of the melt pool in single stripe than that in a single track. In fact, since the method inherently promotes epitaxial crystal growth along the thermal gradient, it is ideal for manufacturing single crystal or columnar grained nickel-based superalloys [53, 54].

Finally, will a defect free TiNb sample built by LPBF be better than that prepared by conventional manufacturing methods in all aspects? From the point of view of cost savings, time savings and customizability, the LPBF built TiNb samples are much better than those manufactured by other conventional means. However, as was noted earlier, there is a large scope to improve the ductility of the material by tailoring the microstructure in a way that mitigates localization from planar slip. One way to achieve that is to develop an equiaxed and fine grained microstructure by tweaking the printing strategy. An alternate way to improve

strain hardening, without modifying the columnar microstructure, is to destabilize the β phase further so that profuse twinning occurs, which in turn promotes increased interactions between dislocations. Also, it is not clear whether alloys manufactured by this strategy will have better structural integrity than that of the conventionally manufactured ones, as their fracture toughnesses and fatigue strengths have not yet been evaluated or compared.

5. Conclusions

With the objective of minimizing the porosity and unmelted Nb inclusions in LPBF built Ti34Nb, three sets of processing parameters, in which P, V_L and laser profile were varied, were used to print samples. After detailed microstructural investigations followed by simulations and mechanical property evaluation of these samples, the following are the key conclusions drawn from this study. The combination of high P (~650 W or 950W), high V_L (~650 mm/s or 950 mm/s), a top-hat profile laser and a suitable stripe scanning strategy is ideal for printing a fully dense sample with limited content of unmelted Nb inclusions. These parameters result in a slow moving, large melt pool, with a small aspect ratio and melt pool angle, in a single stripe. This ensures uniform mixing of constituents and also eliminates keyhole porosities. In addition, these samples have a {100} textured columnar β-Ti microstructure with a few randomly oriented stray grains. The proportion of stray grains increases with Nb content as it is an inoculant for heterogeneous nucleation. Since a stronger {100} texture yields the optimum combination of low E, a lower unmelted Nb inclusion content is desirable. However, irrespective of the Nb inclusion content, the ductility and strain hardening ability of the alloys are sub-par as planar slip in β-Ti occurs without hinderance, leading to flow localization. Further studies are required to develop strategies that homogenize deformation and mitigate planar slip in LPBF printed TiNb, without compromising the strength or E. The broader implication of the study is that the porosity-inclusion dilemma can be resolved by adopting a parameter optimization strategy, which prioritizes ideal melt pool characteristics in a single

stripe as opposed to those in a single track. This is expected to inspire a paradigm shift in devising processing windows that can minimize or completely eliminate defects in materials manufactured via LPBF methods.

6. Acknowledgements

This research is supported by the National Research Foundation, Prime Minister's Office, Singapore under its Medium-Sized Centre funding scheme. S. Huang would like to acknowledge Nanyang President's Graduate Scholarship from Nanyang Technological University for funding the Ph.D. studies. The authors gratefully acknowledge the individuals who served as reviewers for this paper, for their excellent and constructive inputs that significantly improved the quality of the manuscript.

References

[1] M. Ridzwan, S. Shuib, A. Hassan, A. Shokri, M.M. Ibrahim, Problem of stress shielding and improvement to the hip implant designs: a review, J. Med. Sci 7(3) (2007) 460-467.

[2] J. Wolff, Das gesetz der transformation der knochen, A Hirshwald 1 (1892) 1-152.

[3] M. Niinomi, Recent metallic materials for biomedical applications, Metallurgical and Materials Transactions A 33(3) (2002) 477.

[4] K.L. Wapner, Implications of metallic corrosion in total knee arthroplasty, Clinical orthopaedics and related research (271) (1991) 12-20.

[5] S. Hanada, N. Masahashi, T.K. Jung, Effect of stress-induced α″ martensite on Young's modulus of β Ti–33.6Nb–4Sn alloy, Materials Science and Engineering: A 588 (2013) 403-410.

[6] S. Guo, Q. Meng, X. Zhao, Q. Wei, H. Xu, Design and fabrication of a metastable β-type titanium alloy with ultralow elastic modulus and high strength, Scientific Reports 5 (2015) 14688.

[7] Y. Li, C. Yang, H. Zhao, S. Qu, X. Li, Y. Li, New developments of Ti-based alloys for biomedical applications, Materials 7(3) (2014) 1709-1800.

[8] P. Kumar, O. Prakash, U. Ramamurty, Micro-and meso-structures and their influence on mechanical properties of selectively laser melted Ti-6Al-4V, Acta Materialia 154 (2018) 246-260.

[9] P. Kumar, U. Ramamurty, Microstructural optimization through heat treatment for enhancing the fracture toughness and fatigue crack growth resistance of selective laser melted Ti6Al4V alloy, Acta Materialia 169 (2019) 45-59.

[10] P. Kumar, U. Ramamurty, High cycle fatigue in selective laser melted Ti-6Al-4V, Acta Materialia 194 (2020) 305-320.

[11] C. Han, Q. Fang, Y. Shi, S.B. Tor, C.K. Chua, K. Zhou, Recent Advances on High-Entropy Alloys for 3D Printing, Advanced Materials (2020) 1903855.

[12] J. Suryawanshi, K.G. Prashanth, S. Scudino, J. Eckert, O. Prakash, U. Ramamurty, Simultaneous enhancements of strength and toughness in an Al-12Si alloy synthesized using selective laser melting, Acta Materialia 115 (2016) 285-294.

[13] X. Nie, Z. Chen, Y. Qi, H. Zhang, C. Zhang, Z. Xiao, H. Zhu, Effect of defocusing distance on laser powder bed fusion of high strength Al–Cu–Mg–Mn alloy, Virtual and Physical Prototyping (2020) 1-15.

[14] Y. Yang, C. Lu, S. Peng, L. Shen, D. Wang, F. Qi, C. Shuai, Laser additive manufacturing of Mg-based composite with improved degradation behaviour, Virtual and Physical Prototyping (2020) 1-16.

[15] S. Huang, S.L. Sing, W.Y. Yeong, Selective Laser Melting of Ti42Nb Composite Powder and the Effect of Laser Re-Melting, Key Engineering Materials 801 (2019) 270-275.

[16] S.L. Sing, F.E. Wiria, W.Y. Yeong, Selective laser melting of titanium alloy with 50 wt% tantalum: Effect of laser process parameters on part quality, International Journal of Refractory Metals and Hard Materials 77 (2018) 120-127.

[17] S.L. Sing, F.E. Wiria, W.Y. Yeong, Selective laser melting of lattice structures: A statistical approach to manufacturability and mechanical behavior, Robotics and Computer-Integrated Manufacturing 49 (2018) 170-180.

[18] S.L. Sing, W.Y. Yeong, F.E. Wiria, Selective laser melting of titanium alloy with 50 wt% tantalum: Microstructure and mechanical properties, Journal of Alloys and Compounds 660 (2016) 461-470.

[19] R. Martinez, I. Todd, K. Mumtaz, In situ alloying of elemental Al-Cu12 feedstock using selective laser melting, Virtual and Physical Prototyping 14(3) (2019) 242-252.

[20] W. Chen, C. Chen, X. Zi, X. Cheng, X. Zhang, Y.C. Lin, K. Zhou, Controlling the microstructure and mechanical properties of a metastable β titanium alloy by selective laser melting, Materials Science and Engineering: A 726 (2018) 240-250.

[21] M. Fischer, D. Joguet, G. Robin, L. Peltier, P. Laheurte, In situ elaboration of a binary Ti–26Nb alloy by selective laser melting of elemental titanium and niobium mixed powders, Materials Science and Engineering: C 62 (2016) 852-859.

[22] E.G. Brodie, A.E. Medvedev, J.E. Frith, M.S. Dargusch, H.L. Fraser, A. Molotnikov, Remelt processing and microstructure of selective laser melted Ti25Ta, Journal of Alloys and Compounds 820 (2020) 153082.

[23] W.E. King, H.D. Barth, V.M. Castillo, G.F. Gallegos, J.W. Gibbs, D.E. Hahn, C. Kamath, A.M. Rubenchik, Observation of keyhole-mode laser melting in laser powder-bed fusion additive manufacturing, Journal of Materials Processing Technology 214(12) (2014) 2915-2925.

[24] T. Mishurova, K. Artzt, J. Haubrich, G. Requena, G. Bruno, New aspects about the search for the most relevant parameters optimizing SLM materials, Additive Manufacturing 25 (2019) 325-334.

[25] L.G. Hector, R.B. Hetnarski, - Thermal Stresses in Materials Due to Laser Heating, in: R.B. Hetnarski (Ed.), Thermal Stresses IV, North-Holland, Amsterdam, 1996, pp. 453-531.

[26] A.K. Mishra, A. Aggarwal, A. Kumar, N. Sinha, Identification of a suitable volumetric heat source for modelling of selective laser melting of Ti6Al4V powder using numerical and experimental validation approach, The International Journal of Advanced Manufacturing Technology 99(9) (2018) 2257-2270.

[27] J. Yin, H. Zhu, L. Ke, W. Lei, C. Dai, D. Zuo, Simulation of temperature distribution in single metallic powder layer for laser micro-sintering, Computational Materials Science 53(1) (2012) 333-339.

[28] L.-E. Loh, C.-K. Chua, W.-Y. Yeong, J. Song, M. Mapar, S.-L. Sing, Z.-H. Liu, D.-Q. Zhang, Numerical investigation and an effective modelling on the Selective Laser Melting (SLM) process with aluminium alloy 6061, International Journal of Heat and Mass Transfer 80 (2015) 288-300.

[29] M.A. Surmeneva, A. Koptyug, D. Khrapov, Y.F. Ivanov, T. Mishurova, S. Evsevleev, O. Prymak, K. Loza, M. Epple, G. Bruno, In situ synthesis of a binary Ti–10at% Nb alloy by electron beam melting using a mixture of elemental niobium and titanium powders, Journal of Materials Processing Technology 282 (2020) 116646.

[30] R. Laquai, B.R. Müller, G. Kasperovich, G. Requena, J. Haubrich, G. Bruno, Classification of Defect Types in SLM Ti-6Al-V4 by X-ray Refraction Topography, Materials Performance and Characterization 9(1) (2020) 82-93.

[31] B. Vrancken, L. Thijs, J.P. Kruth, J. Van Humbeeck, Microstructure and mechanical properties of a novel β titanium metallic composite by selective laser melting, Acta Materialia 68 (2014) 150-158.

[32] D. Doraiswamy, S. Ankem, The effect of grain size and stability on ambient temperature tensile and creep deformation in metastable beta titanium alloys, Acta Materialia 51(6) (2003) 1607-1619.

[33] J.C. Wang, Y.J. Liu, P. Qin, S.X. Liang, T.B. Sercombe, L.C. Zhang, Selective laser melting of Ti–35Nb composite from elemental powder mixture: Microstructure, mechanical behavior and corrosion behavior, Materials Science and Engineering: A 760 (2019) 214-224.

[34] A.A. Martin, N.P. Calta, S.A. Khairallah, J. Wang, P.J. Depond, A.Y. Fong, V. Thampy, G.M. Guss, A.M. Kiss, K.H. Stone, C.J. Tassone, J. Nelson Weker, M.F. Toney, T. van Buuren, M.J. Matthews, Dynamics of pore formation during laser powder bed fusion additive manufacturing, Nature Communications 10(1) (2019) 1987.

[35] D. Zhao, C. Han, J. Li, J. Liu, Q. Wei, In situ fabrication of a titanium-niobium alloy with tailored microstructures, enhanced mechanical properties and biocompatibility by using selective laser melting, Materials Science and Engineering: C (2020) 110784.

[36] P. Tang, S. Wang, H. Duan, M. Long, Y. Li, S. Fan, D. Chen, The Formation of Humps and Ripples During Selective Laser Melting of 316l Stainless Steel, JOM 72(3) (2020) 1128-1137.

[37] C. Tang, K.Q. Le, C.H. Wong, Physics of humping formation in laser powder bed fusion, International Journal of Heat and Mass Transfer 149 (2020) 119172.

[38] Z. Sun, X. Tan, S.B. Tor, C.K. Chua, Simultaneously enhanced strength and ductility for 3D-printed stainless steel 316L by selective laser melting, NPG Asia Materials 10(4) (2018) 127-136.

[39] R. Hermann, H. Hermann, M. Calin, B. Büchner, J. Eckert, Elastic constants of single crystalline β-Ti70Nb30, Scripta Materialia 66(3-4) (2012) 198-201.

[40] H.Y. Kim, Y. Ikehara, J.I. Kim, H. Hosoda, S. Miyazaki, Martensitic transformation, shape memory effect and superelasticity of Ti–Nb binary alloys, Acta Materialia 54(9) (2006) 2419-2429.

[41] S.S.S. Kumar, B. Pavithra, V. Singh, P. Ghosal, T. Raghu, Tensile anisotropy associated microstructural and microtextural evolution in a metastable beta titanium alloy, Materials Science and Engineering: A 747 (2019) 1-16.

[42] A. Gysler, G. Lütjering, V. Gerold, Deformation behavior of age-hardened Ti-Mo alloys, Acta Metallurgica 22(7) (1974) 901-909.

[43] S.L. Sing, W.Y. Yeong, F.E. Wiria, Selective laser melting of titanium alloy with 50 wt% tantalum: Microstructure and mechanical properties, Journal of Alloys and Compounds 660 (2016) 461-470.

[44] S. Huang, S.L. Sing, G. Delooze, R. Wilson, W.Y. Yeong, Laser powder bed fusion of titanium-tantalum alloys: Compositions and designs for biomedical applications, Journal of the Mechanical Behavior of Biomedical Materials (2020) 103775.

[45] W. Kurz, B. Giovanola, R. Trivedi, Theory of microstructural development during rapid solidification, Acta Metallurgica 34(5) (1986) 823-830.

[46] J.D. Hunt, Steady state columnar and equiaxed growth of dendrites and eutectic, Materials Science and Engineering 65(1) (1984) 75-83.

[47] V. Fallah, Solidification in laser powder deposition of Ti-Nb alloys, (2011).

[48] J.W. Aveson, P.A. Tennant, B.J. Foss, B.A. Shollock, H.J. Stone, N. D'Souza, On the origin of sliver defects in single crystal investment castings, Acta Materialia 61(14) (2013) 5162-5171.

[49] J. Aveson, G. Reinhart, H. Nguyen-Thi, N. Mangelinck-Noël, N. d'Souza, H. Stone, Origins of misorientation defects in single crystal castings: A time resolved in situ synchrotron X-ray radiography study, MATEC Web of Conferences, EDP Sciences, 2014, p. 05003.

[50] J.W. Aveson, G. Reinhart, C.J.L. Goddard, H. Nguyen-Thi, N. Mangelinck-Noël, A. Tandjaoui, J.R. Davenport, N. Warnken, F. di Gioacchino, T.A. Lafford, N. D'Souza, B. Billia, H.J. Stone, On the Deformation of Dendrites During Directional Solidification of a Nickel-Based Superalloy, Metallurgical and Materials Transactions A 50(11) (2019) 5234-5241.

[51] L.-C. Chuang, K. Maeda, H. Morito, K. Shiga, K. Fujiwara, Origin of small-angle grain boundaries during directional solidification in multicrystalline silicon, Materialia 3 (2018) 347-352.

[52] H. Schwab, F. Palm, U. Kühn, J. Eckert, Microstructure and mechanical properties of the near-beta titanium alloy Ti-5553 processed by selective laser melting, Materials & Design 105 (2016) 75-80.

[53] D. Schwarze, J. Chen, Method and apparatus for producing a single-crystalline workpiece, Google Patents, 2019.

[54] Y. Li, K. Chen, R.L. Narayan, U. Ramamurty, Y. Wang, J. Long, N. Tamura, X. Zhou, Multi-scale microstructural investigation of a laser 3D printed Ni-based superalloy, Additive Manufacturing 34 (2020) 101220.